(I) THE SIGNIFICANCE OF INCORPORATING A 3D POINT SOURCE IN INVERSE SCATTERING SERIES (ISS) MULTIPLE REMOVAL FOR A 1D/2D SUBSURFACE; (II) AN ALTERNATIVE ISS INTERNAL MULTIPLE ELIMINATION ALGORITHM FOR THE FIRST-ORDER INTERNAL MULTIPLES HAVING THEIR DOWNWARD REFLECTION AT THE OCEAN BOTTOM

A Dissertation Presented to

the Faculty of the Department of Physics

University of Houston

In Partial Fulfillment

of the Requirements for the Degree

Doctor of Philosophy

By

Xinglu Lin

August 2016

(I) THE SIGNIFICANCE OF INCORPORATING A 3D POINT SOURCE IN INVERSE SCATTERING SERIES (ISS) MULTIPLE REMOVAL FOR A 1D/2D SUBSURFACE; (II) AN ALTERNATIVE ISS INTERNAL MULTIPLE ELIMINATION ALGORITHM FOR THE FIRST-ORDER INTERNAL MULTIPLES HAVING THEIR DOWNWARD REFLECTION AT THE OCEAN BOTTOM

Xinglu Lin

APPROVED:

Dr. Arthur B. Weglein, Chairman

Dr. Mini Das

Dr. Fang Liu

Dr. David J. Francis

Dr. Jingfeng Zhang

Dr. Hong Liang

Dean, College of Natural Sciences and Mathematics

Acknowledgements

The research described in this dissertation proceeds from fall of 2013 to summer of 2016. I am writing here to express my gratitude to many people who support this research. Firstly, I would like to especially thank Prof. Arthur B. Weglein for being my dissertation advisor and supporting the project all the time. I enjoy the great benefit of his technical knowledge and deep thoughts. And I owe great gratitude to Prof. Fang Liu, Prof. Mini Das, Prof. David Francis, Dr. Jingfeng Zhang, and Dr. Hong Liang for serving as my committee members. Also, I appreciate the help through this project from all my wonderful colleagues in M-OSRP group, who are all team-oriented and capable, particularly Jing Wu, Chao Ma, Qiang Fu, Jinglong Yang, and Lin Tang for being great friends and work partners.

My special thanks also go to my family and all my friends, especially my husband Zhao Li. I would not have been able to complete this dissertation without their continuous love and encouragement in difficult time.

Finally, I want to express heartfelt thanks to my parents, for their support and patience all the time. Distance between us cannot change the distance between our hearts. I receive meticulous care from them all the time.

(I) THE SIGNIFICANCE OF INCORPORATING A 3D POINT SOURCE IN INVERSE SCATTERING SERIES (ISS) MULTIPLE REMOVAL FOR A 1D/2D SUBSURFACE; (II) AN ALTERNATIVE ISS INTERNAL MULTIPLE ELIMINATION ALGORITHM FOR THE FIRST-ORDER INTERNAL MULTIPLES HAVING THEIR DOWNWARD REFLECTION AT THE OCEAN BOTTOM

An Abstract of a Dissertation

Presented to

the Faculty of the Department of Physics

University of Houston

In Partial Fulfillment

of the Requirements for the Degree

Doctor of Philosophy

By

Xinglu Lin

August 2016

Abstract

Inverse scattering series (ISS) de-multiple methods do not require any subsurface information to achieve seismic processing objectives. In specific applications of the ISS de-multiple methods, the subsurface is assumed to 1D, 2D, or 3D and the dimension of the source is typically chosen to agree with the dimension of the subsurface, for example, choosing a 2D line source for a 2D subsurface. And often in deriving a 1D subsurface theory from a 2D algorithm the 2D line source is brought along into the 1D subsurface theory. However, field data are generated by a locally 3D source and realistic synthetic data need to incorporate a 3D source. The lesson is that there are times when a 1D or 2D subsurface can be a reasonable approximation, but it is always important to incorporate a 3D source to have an effective multiple predictor and removal. This dissertation describes how to incorporate a 3D source in ISS de-multiple methods for a 1D and 2D subsurface. We then evaluate the positive added value of incorporating a 3D source in the distinct 1D subsurface algorithms, using synthetic data generated by a 3D source.

The second part provides an approach to address the challenge of current internal multiple attenuator. The current algorithm provides accurate time and approximate amplitude of all internal multiples. For complex circumstances, where internal multiples are often proximal to or interfering with primaries, the current ISS internal multiple attenuator plus an adaptive subtraction can fail to remove multiples without damaging primaries. This challenge demands an internal multiple eliminator, in which both time and amplitude of internal multiples can be accurately predicted. There are circumstances where it is possible to provide reliable subsurface information to transform the internal multiple attenuator into an eliminator. For example,

in marine exploration, the earth properties down to and across the ocean bottom can often be estimated from a velocity analysis. With that information, the ISS internal multiple attenuator can eliminate all internal multiples having their shallowest downward reflection at the ocean bottom. The effectiveness of the proposed method is evaluated by a 1D normal incidence test.

Contents

List of Figures

Chapter 1

Introduction and Background

This chapter briefly introduces the seismic experiment/acquisition, definitions of seismic events, and a typical seismic processing chain. In addition, certain challenges and corresponding strategies are discussed to provide a better understanding of the contributions in this dissertation. The last section in this chapter provides an overview of this dissertation.

1.1 General introduction to seismic exploration

The objective of seismic exploration is to determine subsurface information from the recorded seismic reflection data by applying different mathematical and physical tools to estimate rock and fluid properties. The ultimate goal is to locate and analyze hydrocarbon reservoirs[1] in the earth.

1.1.1 Seismic acquisition

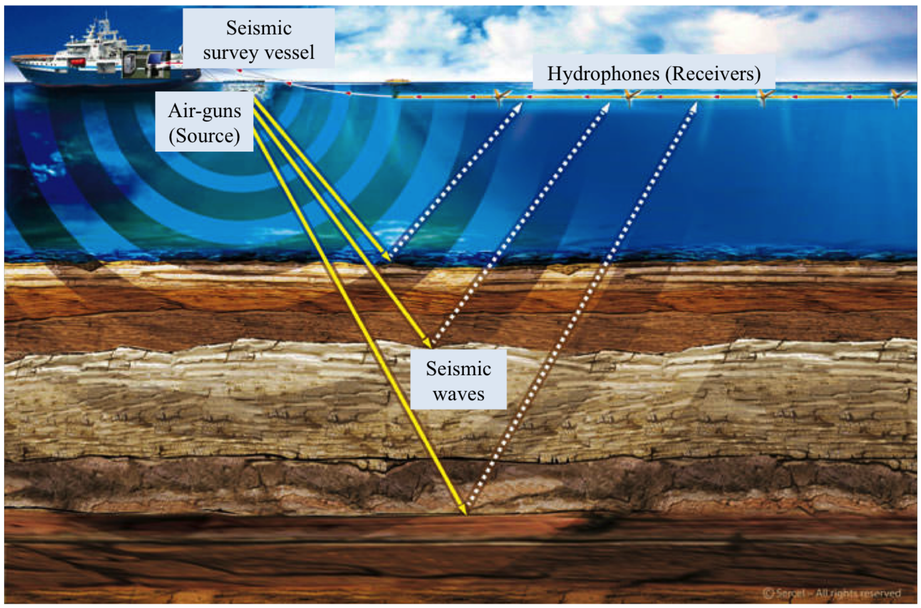

Figure 1.1: Marine acquisition (http://www.sercel.com)

Seismic experiment/acquisition starts from a man-made source, which could explode in the water column (e.g., air-gun for marine plays) or on the surface of earth (e.g., Vibroseis for onshore) or near the surface of earth (e.g., dynamite for onshore). This explosion generates waves that propagate in the subsurface. When a seismic wave traveling through the earth encounters a reflector (a rapid change of earth properties) between two materials with different impedances, part of the wave energy is reflected

[1]A petroleum reservoir is a subsurface pool of hydrocarbons contained in porous or fractured rock formations.

off the reflector and is detected by an array of seismic receivers[2]. As an example of seismic acquisition, a marine acquisition is seen in Figure 1.1, where a vessel is towing air-guns and hydrophone streamers that move in the ocean environment for repeated measurements.

1.1.2 Definitions of seismic events

For a given source, the seismic energy recorded by one receiver produces a time sequence of different arrivals (which is defined as a seismic trace). These distinct arrivals are called seismic events, which are temporally localized. Due to their different experiences in the subsurface, seismic events can be categorized into different types. A cartoon in figure 1.2 shows the events in different categories in terms of their history. The air-water boundary is defined as a free surface. The categories are defined in sequence, where the first class contains reference waves, ghosts, primaries, and multiples.

(1) Reference wave. Instead of describing the actual medium directly, perturbation theory is used to separate the actual medium into a reference medium plus a perturbation. The choice of a reference medium depends on the specific seismic objective and application. Waves that propagate in the reference medium are called reference waves. The waves that travel in the actual medium are called actual waves. The difference between the actual and reference waves is defined as the scattered wave. For separating the reference wave and scattered wave in marine application,

[2] A seismic receiver is a device that record the seismic wave energy in the form of a ground motion (e.g., geophone) or a pressure wave in the fluid (e.g., hydrophone) and transforms it into an electrical impulse.

a half-space of air plus a half-space of water can be selected as a reference medium. As a consequence, the reference wave contains a direct wave (solid green line), which travels directly from the source to the receiver, and a downward reflection of the direct wave at the free surface (dash green line), which starts the history from the source upward, hits the free surface, and then reaches the receiver. For this reference medium, the events in the reference wave do not experience the earth; hence, they do not carry subsurface information. However, the reference wave contains information of the source signature and radiation pattern.

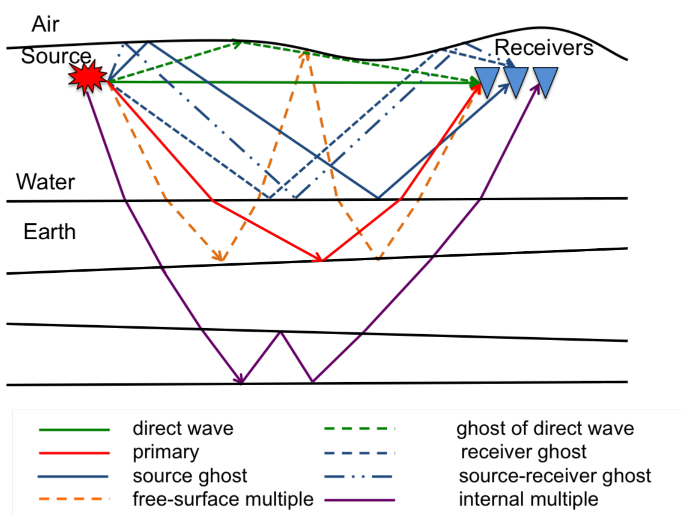

Figure 1.2: Marine-seismic events

The parts of the wave that has experienced contact with the earth are further separated by the direction the event was moving when it left the source and the direction the event was moving when it was recorded:

(2) Ghosts. Ghost events are defined as the seismic events that begin their history by traveling up from source to the free surface or end their history by traveling down

from free surface to the receiver or both. This type of events can be further described as source-side ghost[3] (Figure 1.2, solid blue line), receiver-side ghost [4] (Figure 1.2, dash blue line) and source-receiver-side ghost[5] (Figure 1.2, dash-dot blue line).

After defining a ghost, the events that begin their history by downward travel from source and end their history by upward travel to the receiver can be further classified from their history in the subsurface as follows:

(3) Primary. The primaries are events that experience only one upward reflection from the subsurface as seen by the solid red line in figure 1.2.

(4) Multiple. In contrast to a primary event, a multiple is defined as an event that has been upward reflected multiple times and downward reflected at least once. Depending on the location of the downward reflection, multiple events can be divided into two categories, free-surface multiple (dash orange line) and internal multiple (solid purple line). As seen in Figure 1.2, a free-surface multiple has at least one downward reflection at the free surface for a marine measurement (or air-land boundary for onshore), whereas an internal multiple has all of its downward reflections occur below the free surface. Both free-surface and internal multiples can be classified into different orders. The order of a free-surface multiple is defined by the total number of downward reflections at the free surface or the air-land boundary. And the order of an internal multiple is determined by the total number of the downward reflections

[3] Source-side ghost is the event that starts its propagation history by traveling up from the source and then reflecting down by the free surface.

[4] Receiver-side ghost is the event that ends its propagation history by reflecting down by the free surface and then traveling down to the receiver.

[5] Source-receiver-side ghost is the event that carries both the features of source-side ghost and receiver-side ghost.

at any subsurface reflector in its traveling history.

1.1.3 A typical processing chain and corresponding tools

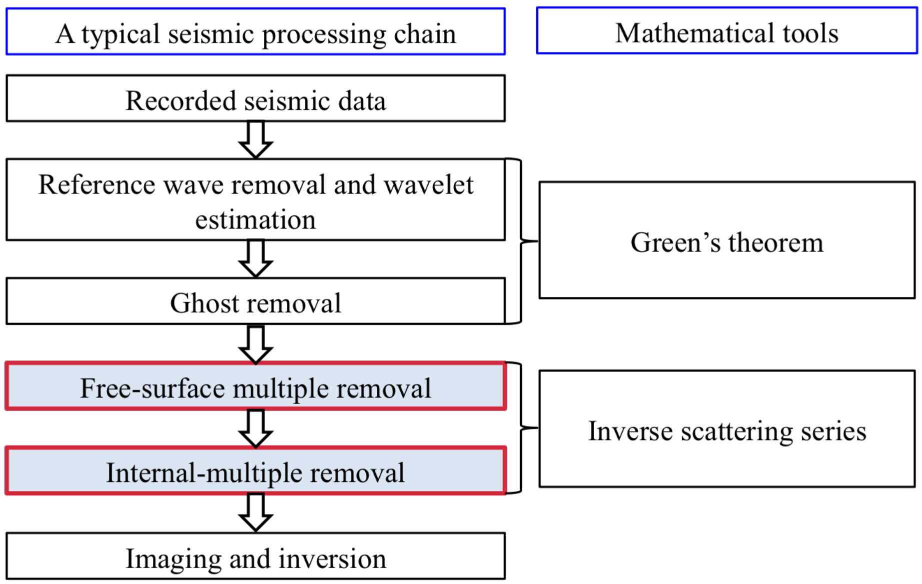

Figure 1.3: A typical seismic processing chain and corresponding mathematical tools. This dissertation focuses on the highlighted steps (red box): free-surface multiple removal and internal multiple removal.

One of the ultimate purposes in seismic exploration is to know where the reflectors are located in the subsurface and how the properties change across these reflectors. The goal of imaging is to locate subsurface reflectors, and inversion aims to delineate the change of properties in the subsurface. Both conventional imaging and inversion methods assume seismic data consists of only primaries. However, the primary-only data are not the total recorded seismic data that often contain a wide range of events.

This primary-only assumption demands a series of processing to remove the undesired events (e.g., reference waves, ghosts, and multiples). A typical and simplified processing chain and the corresponding mathematical tools are illustrated in figure 1.3, where the highlighted parts in red boxes are the topics advanced by this dissertation. This specific chain can be classified into two categories, (1) preprocessing (e.g., reference wave removal, wavelet estimation, and ghost removal) and (2) processing (e.g., multiple removal, imaging, and inversion). The details of each stage and the corresponding concepts are discussed below.

The first stage called preprocessing includes (1) identifying and removing the reference wave, (2) estimating the source signature and radiation pattern from the reference wave, and (3) deghosting.

For a marine application, as discussed in section 1.1.2, the reference wave includes the direct wave and the downward reflection of the direct wave at the free surface. Due to the traveling history of the reference wave, it contains the information on the source signature and radiation pattern, but no subsurface information. On one hand, the objective of wavelet estimation[6] can be achieved by identifying the reference wave. On the other hand, imaging and inversion can benefit from removing the reference wave. Thereby, it is useful to identify the reference wave (for wavelet estimation) and remove the reference wave (for the subsequent steps) before the remaining analysis. After accomplishing the reference wave removal and wavelet estimation, the data will have ghosts. Ghosts lead to notches in the data spectrum, which can generate

[6] Wavelet estimation can provide the source signature with radiation pattern plus, e.g., all factors that are outside the assumed physics of the subsurface and acquisition, for example, instrument response.

a serious issue in Amplitude-Versus-Offset analysis (Zhang, 2007). The reason is that ghost notches result from the destructive interference between up- and down-going waves. Therefore, part of the frequency in the source can be destroyed in the recorded seismic data due to the interference of a reflection wave and its ghost. Removing ghosts can boost the low-frequency information and remove the notches in data spectrum; hence, it can improve the resolution of the seismic data. The stage of preprocessing delivers the prerequisites of subsequent multiple removal, imaging, and inversion.

The second stage is the process of removing multiples, imaging, and inversion. Among typical imaging methods, there are two available imaging principles. One is defined as Claerbout II (CII) imaging principle (Claerbout, 1971; Baysal et al., 1983; Whitmore, 1983; McMechan, 1983), which is considered as the industry standard imaging principle. This standard imaging principle is based on a space-time coincidence of up- and down-going waves. The other newly developed imaging principle is defined as Claerbout III (CIII) imaging principle (Weglein et al., 2011a,b; Liu and Weglein, 2014). CIII imaging predicts what a source and receiver would record inside the earth, then arranges the predicted source and receiver to be coincident and asks for $t = 0$. Both of them request a velocity model as input. Weglein (2016) concludes that by choosing an accurate and discontinuous velocity model in CIII, multiples would not contribute to the imaging of a geological structure. However, if a smooth and continuous velocity model (i.e., generally assumed in practice) is chosen, each multiple will result in a false, misleading, and potentially injurious subsurface image and should be removed before imaging. In practice, we image with a smooth velocity model, and hence multiples (free-surface multiples and internal multiples) must be removed.

The mission-oriented seismic research program (M-OSRP) pioneered and developed two basic mathematical tools (Figure 1.3) that provide a framework for a seismic-data processing chain. The tools are Green's theorem and the sub-series in inverse scattering series (ISS). Among the ISS methods, which can achieve the seismic objectives without any subsurface information, the free-surface multiple elimination and internal multiple attenuation algorithms are advanced in this dissertation.

1.2 Challenges and strategy

Many seismic processing methods require subsurface information to be effective. As the petroleum industry moves to more complex offshore and onshore locations, that requirement can be increasingly difficult to satisfy, leading to processing and drilling failures. The Inverse Scattering Series (ISS) communicates that all seismic processing objectives can be achieved directly and without subsurface information. Among seismic processing objectives are: (1) the removal of reference wave, (2) deghosting, (3) multiple removal, and (4) imaging and inverting primaries. The seismic processing task this dissertation focuses on is multiple removal.

Since ISS de-multiple methods are a subseries of the ISS. These methods do not require subsurface information. However, general challenges and open issues still exist in ISS multiple removal. These have been addressed by a comprehensive three-pronged strategy (Weglein, 2014):

1. The improvement of current preprocessing methods for both offshore play (e.g., reference wave removal, wavelet/radiation pattern estimation, and deghosting) and onshore play (e.g., ground roll removal) to provide satisfactory prerequisites;

2. The development of the ISS internal multiple elimination algorithm and enhancing the effectiveness of current ISS-multiple removal methods;

3. The Building of an alternative criteria for adaptive subtraction, derived from and serves the ISS free-surface and internal multiple removal.

This three-pronged strategy represents a consistent and aligned processing chain, which provides a direct and practical solution to the removal of all multiple without damaging the primaries. This section describes two certain concerns in the ISS de-multiple methods. This dissertation discusses and addresses each of them, thus being a part of the three-pronged strategy.

In specific applications of the ISS methods for free-surface and internal multiples, the subsurface is assumed to 1D, 2D, or 3D and the dimension of the source is typically chosen to agree with the dimension of the subsurface, for example, choosing a 2D line source for a 2D-subsurface. And often in deriving a 1D subsurface theory from a 2D algorithm the 2D line source is brought along into the 1D-earth varying theory. Field data is generated by a locally 3D-source and realistic synthetic data tests need to incorporate a 3D-point like source to be effective and realistic. This dissertation describes how to incorporate a 3D point source in ISS de-multiple methods for 1D and 2D subsurfaces. The lesson of this dissertation is that there are times when a 1D or 2D subsurface can be a useful and is a reasonable approximation, but it is always important to incorporate a 3D-source to have an effective multiple predictor and removal.

The second part of this dissertation addresses an open issue of the current internal multiple attenuator. The current algorithm provides accurate time and approximate amplitudes of all internal multiples. For complex circumstances, where internal multiples are often proximal to or interfering with primaries, the current ISS internal multiple attenuator plus an adaptive subtraction may not remove multiples without damaging the primaries. This issue demands an internal multiple eliminator, in which both time and amplitudes of internal multiples can be accurately predicted. There are circumstances where it is possible to provide reliable and accurate subsurface information to transform the ISS internal multiple attenuator into an eliminator. For example, in marine exploration, the earth properties down to and across the ocean bottom can often be well-estimated from a conventional velocity analysis. With that information, the ISS internal multiple attenuator can eliminate all internal multiples that have their shallowest downward reflector at the ocean bottom.

The topics discussed in this dissertation provide two advances to the capabilities of ISS de-multiple methods by (1) adding the physics of a realistic 3D source to enhance the effectiveness within current ISS methods; (2) in a further step, utilize the achievable subsurface information to develop an internal multiple eliminator.

1.3 Overview of this dissertation

Chapter 1 reviews the general background of seismic exploration and specific challenges of ISS de-multiple methods addressed by this dissertation.

Chapter 2 explains how to incorporate a 3D point source in the ISS free-surface multiple elimination algorithm for a 1D subsurface. The difference a 3D point source assumption can make, comparing to a frequently used 2D line source assumption, is exemplified and analyzed on realistic synthetic data generated by a 3D point source and a 1D subsurface.

Chapter 3 focuses on the effect of incorporating a 3D point source in the ISS internal multiple attenuation algorithm for a 1D/2D subsurface. First, a realistic 3D point source is added for a 1D-earth ISS internal multiple prediction theory by starting from a complete 3D theory and then reducing the earth dimension from 3D to 1D. The significance has been shown by comparing internal multiple predictions assuming a 2D line source versus a 3D point source for synthetic 3D-source data. Second, the negative consequence of mismatching source dimension in free-surface multiple removal to the subsequent internal multiple prediction is exemplified. As an extension, a 2D-earth ISS internal multiple attenuator accommodating a 3D point source is also advanced and analyzed.

Chapter 4 provides a way to eliminate a specific but important class of internal multiples, by directly giving the information of a specific attenuation factor[7]. Instead

[7]Attenuation factor is defined as the difference between current internal multiple prediction (from attenuation algorithm) and actual-internal multiple.

of extracting the attenuation factor from reflection data (Herrera and Weglein, 2012; Zou and Weglein, 2014; Zou et al., 2016), the attenuation factor can be found by velocity analysis of the ocean bottom in a typical marine exploration. For those internal multiples having only one downward reflection at the ocean bottom, an alternative ISS internal multiple eliminator can be achieved with the knowledge of the properties down to and across the ocean bottom, independent of how deep and how many layers the internal multiples travel trough. As a preliminary study, a 1D-normal incidence test is designed and performed to evaluate the effectiveness of the proposed ISS internal multiple eliminator.

Chapter 5 summarizes the contributions of this dissertation.

Chapter 2

Incorporating a 3D point source in ISS free-surface multiple elimination (FSME) algorithm for a 1D subsurface

Based on the current 3D-inverse scattering series (ISS) free-surface multiple elimination (FSME) algorithm (Carvalho, 1992; Weglein et al., 1997, 2003) that was developed for a 3D point source and 3D earth, this chapter derives an ISS FSME algorithm that retains the dimension of the source (i.e., 3D point source) and reduces the subsurface dimension from 3D to 1D. Numerical tests were performed on 3D source synthetic data generated from a 1D subsurface, to examine the significance of incorporating a 3D source in FSME algorithm, compared to a frequently used 2D line source algorithm (i.e., 1.5D algorithm). The results demonstrate that the 3D source/1D subsurface ISS FSME algorithm can completely remove the free-surface multiples in 3D source data. This successful removal of free-surface multiples provides a satisfactory prerequisite for subsequent processing (e.g., internal multiple attenuation/elimination).

2.1 Introduction

Multiple removal is a long-standing and challenging task in seismic data processing, which impacts the subsequent imaging and inversion procedures. Many efforts have been made to attenuate or eliminate the free-surface multiples (events that have experienced at least one downward reflection at the air-water surface) in data (e.g., Verschuur et al., 1992; Carvalho, 1992; Weglein et al., 1997, 2003; Weglein and Dragoset, 2008). Among these methods, the inverse scattering series (ISS) free-surface multiple elimination (FSME) algorithm provides a multidimensional procedure that eliminates all free-surface multiples (Carvalho, 1992; Weglein et al., 1997, 2003) through a simple subtraction. This approach has its strengths in that it does not require subsurface information, and it can provide the accurate time and amplitude of all free-surface multiples. However, other approaches, such as the surface-related multiple elimination (SRME) method, often adopt adaptive subtraction with certain criteria (e.g., energy minimization) to eliminate the free-surface multiples, because these methods can provide accurate time but approximate amplitude of free-surface multiples. Adaptive subtraction works well at times when the events are isolated, however, it can generate issues when the free-surface multiples and primaries are interfering or destructively overlapping. This is because energy minimization assumes a minimized/decreased energy in data after multiple subtraction, which is invalid when the energy increases after removing destructively overlapping free-surface multiples and at the same time recovering the primaries. In other words, for a complex geology, it is in need of accurate free-surface multiple predictions for both time and amplitude, where the adaptive subtraction can fail to effectively remove the free-surface multiples and can possibly damage the primaries.

As we mentioned before, the ISS FSME algorithm is a multidimensional procedure that can completely remove the free-surface multiples from data without knowledge of any subsurface information. If we consider a 3D point source as the real source dimension, the complete 3D ISS FSME algorithm, which assumes a 3D point source and a 3D subsurface, can successfully predict both accurate time and amplitudes of all free-surface multiples with a complete dataset (requires areal coverage of sources and for each source requires the areal coverage of receivers). Even though the 3D ISS FSME algorithm is a complete and accurate method, there are reasonable circumstances that require less data and less computational cost, for instance, when the earth property only varies in 1D and the source dimension retains 3D. For a typical pre-stack shot gather coming from a 1D subsurface, the 1.5D ISS FSME algorithm is frequently and naturally applied to predict free-surface multiples (Carvalho, 1992). Since the 1.5D ISS FSME algorithm assumes a 2D line source, it can only provide the accurate time and amplitude of free-surface multiples generated by a 2D line source, rather than a 3D point source. When the data come from a realistic point source and a 1D subsurface, this 1.5D algorithm can produce issues and even fail to effectively eliminate the free-surface multiples.

This chapter will develop a specific 3D source/1D subsurface ISS FSME algorithm by reducing a complete 3D ISS FSME algorithm. The reduced algorithm preserves the real 3D source dimension and demands only one pre-stack shot gather for the 3D-source data coming from a 1D earth. The numerical tests were performed on 3D-source data. The results evaluated the significance of incorporating a 3D source in free-surface multiple removal by comparing to a frequently used 1.5D algorithm for realistic synthetic data.

2.2 Review of complete 2D and 3D ISS free-surface multiple elimination algorithms

The ISS free-surface multiple elimination algorithm was originally pioneered by Carvalho (1992); Weglein et al. (1997) for 1D, 2D, and 3D world. This multidimensional method will be revisited in this section for 3D and 2D cases.

The preparation of the 3D FSME algorithm starts from data $D(x_g, y_g, \epsilon_g, x_s, y_s, \epsilon_s; t)$, where (x_g, y_g, ϵ_g) and (x_s, y_s, ϵ_s) are the receiver- and source-location, respectively. The depth of sources (ϵ_s) and receivers (ϵ_g) are fixed and known. In addition, the preprocessing - including the reference wave removal, deghosting, and wavelet estimation - needs to be achieved before the ISS free-surface multiple prediction. The preprocessed data are represented by D'. Fourier transform the data D' in the space-time domain to the wavenumber-frequency domain as input $D'_1(k_{xg}, k_{yg}, k_{xs}, k_{ys}; \omega)$. The 3D source ISS free-surface multiple elimination algorithm can be written as

$$D'_n(k_{xg}, k_{yg}, k_{xs}, k_{ys}; \omega) = \frac{1}{2i\pi^2 \rho_r B(\omega)} \int_{-\infty}^{\infty} \int_{-\infty}^{\infty} dk_x dk_y D'_1(k_{xg}, k_{yg}, k_x, k_y; \omega) \times q D'_{n-1}(k_x, k_y, k_{xs}, k_{ys}; \omega) e^{iq(\epsilon_g + \epsilon_s)}, \tag{2.1}$$

for $n \geq 2$ and

$$D'(k_{xg}, k_{yg}, k_{xs}, k_{ys}; \omega) = \sum_{n=1}^{\infty} D'_n(k_{xg}, k_{yg}, k_{xs}, k_{ys}; \omega). \tag{2.2}$$

D' contains only the primaries and internal multiples. $B(\omega)$ and ρ_r are the source signature and reference medium density, respectively. The vertical wavenumber is defined by $q = \text{sgn}(\omega)\sqrt{(\omega/c_0)^2 - k_x^2 - k_y^2}$. The 3D algorithm in equations (2.1) and (2.2) assumes that the acquisition applies 3D point sources and 3D point receivers for a 3D subsurface. The source dimension is always close to 3D in real data.

Similarly, a set of 2D preprocessed data $D'(x_g, x_s; t)$ can be Fourier transformed into the wavenumber-frequency domain as $D'_1(k_g, k_s; \omega)$. The 2D ISS free-surface multiple elimination algorithm is,

$$D'_n(k_g, k_s; \omega) = \frac{1}{i\pi \rho_r B(\omega)} \int_{-\infty}^{\infty} dk D'_1(k_g, k; \omega) q D'_{n-1}(k, k_s; \omega) e^{iq(\epsilon_g + \epsilon_s)}, \tag{2.3}$$

for $n \geq 2$ and

$$D'(k_g, k_s; \omega) = \sum_{n=1}^{\infty} D'_n(k_g, k_s; \omega), \tag{2.4}$$

where the vertical wavenumber is $q = \text{sgn}(\omega)\sqrt{(\omega/c_0)^2 - k^2}$. The algorithm in equations (2.3) and (2.4) assumes an entire 2D world, in which everything is 2D, including source dimension as well as earth dimension.

2.3 Theory

In the following sections, both the 3D and 2D free-surface multiple algorithms are reduced for the data from a 1D subsurface, where in the 3D algorithm the source is assumed to be a 3D point source and in the 2D algorithm the source is assumed to be a 2D line source. For convenience, the superscript $1DE$ represents the 1D earth assumption for different sources (for example, $2D1DE$ represents 2D line source and 1D earth; $3D1DE$ represents 3D point source and 1D earth).

2.3.1 Frequently used 2D line source/1D subsurface ISS FSME algorithm

In developing the algorithm for 1D earth pre-stack data, it was natural that people started with the 2D line source ISS FSME algorithm and then reduced it for a 1D subsurface. The data that occur in a 2D world can be written as $D(x_g, x_s; \omega)$ or $D(x_m, x_h; \omega)$ in the space-frequency domain, where $x_m = x_g + x_s$ and $x_h = x_g - x_s$. The data coming from a 1D earth, shown as $D^{2D1DE}(x_h; \omega)$, depends only on the source-receiver offset (x_h) and the frequency (ω). The Fourier transform over a complete 2D data coming from a 1D earth can be shown as,

$$D(k_g, k_s; \omega) = \iint e^{ik_g x_g} e^{-ik_s x_s} D^{2D1DE}(x_h; \omega) dx_g dx_s. \tag{2.5}$$

Rearranging the variables from (k_g, k_s) to (k_h, k_m) can give us,

$$\begin{aligned} D(k_h, k_m; \omega) &= \frac{1}{2} \int e^{ik_h x_h} D^{2D1DE}(x_h; \omega) dx_h \int e^{ik_m x_m} dx_m \\ &= D^{2D1DE}(k_h; \omega)(2\pi)\delta(2k_m), \end{aligned} \tag{2.6}$$

where $k_h = \frac{k_g+k_s}{2}$ and $k_m = \frac{k_g-k_s}{2}$. The dataset is independent of x_m and it can come out of the x_m integral. Consequently, the Fourier transform integral over x_m can produce a Dirac delta function in k_m. Since the 2D source ISS FSME algorithm needs data in (k_g, k_s), we can change the variables in equation (2.6) back to (k_g, k_s) as,

$$D(k_g, k_s; \omega) = D^{2D1DE}(k_g; \omega)(2\pi)\delta(k_g - k_s), \tag{2.7}$$

where the relation $k_g = k_s = k_m$ is defined by the sifting property of the Dirac delta function.

As part of a complete data set, the preprocessed data D' has the same symmetry as D, which is $D'_n(k_g, k_s; \omega) = D_n'^{2D1DE}(k_g; \omega)(2\pi)\delta(k_g - k_s)$. By applying this 1D earth data $D_n'^{2D1DE}$ to equation (2.1), the algorithm becomes

$$\begin{aligned}
&D_n'^{2D1DE}(k_g; \omega)(2\pi)\delta(k_g - k_s)\\
&= \frac{1}{i\pi\rho_r B(\omega)} \int_{-\infty}^{\infty} dk D_1'^{2D1DE}(k_g; \omega)(2\pi)\delta(k_g - k)\\
&\times q D_{n-1}'^{2D1DE}(k; \omega)(2\pi)\delta(k - k_s) e^{iq(\epsilon_g + \epsilon_s)}.
\end{aligned} \tag{2.8}$$

The lateral integral ($\int dk$) can be evaluated using the Dirac delta functions. Then equation (2.8) produces the reduced 1.5D free-surface multiple eliminator as,

$$\begin{aligned}
&D_n'^{2D1DE}(k_g; \omega)\delta(k_g - k_s)\\
&= \frac{2}{i\rho_r B(\omega)} \delta(k_g - k_s) D_1'^{2D1DE}(k_g; \omega) q D_{n-1}'^{2D1DE}(k_s; \omega) e^{iq(\epsilon_g + \epsilon_s)}.
\end{aligned} \tag{2.9}$$

Integrating over k_g on both sides provides the FSME assuming a 2D line source as

$$D_n'^{2D1DE}(k_h; \omega) = \frac{2}{i\rho_r B(\omega)} D_1'^{2D1DE}(k_h; \omega) q D_{n-1}'^{2D1DE}(k_h; \omega) e^{iq(\epsilon_g + \epsilon_s)}, \tag{2.10}$$

for $n \geq 2$ and $q = \mathrm{sgn}(\omega)\sqrt{(\omega/c_0)^2 - k_h^2}$,

$$D'^{2D1DE}(k_h;\omega) = \sum_{n=1}^{\infty} D_n'^{2D1DE}(k_h;\omega), \tag{2.11}$$

where $k_h = k_g = k_s$ (by evaluating the Dirac delta functions). Free-surface multiple removed data in the space domain can be obtained by an inverse Fourier transform as,

$$D'^{2D1DE}(x_h;\omega) = \frac{1}{2\pi}\int D'^{2D1DE}(k_h;\omega)e^{-ik_hx_h}dk_h. \tag{2.12}$$

The process following equations (2.6), (2.10), (2.11), and (2.12) provides us the ISS FSME algorithm assuming a 2D line source for a 1D subsurface.

2.3.2 Reduced 3D point source/1D subsurface ISS FSME algorithm

3D data generated by a 1D subsurface only depend on the source-receiver offset and the frequency, which is a spatial circular symmetry in cylindrical coordinates (independent of azimuth angle). This symmetry makes it convenient to study the 1D earth problem with cylindrical coordinates, which is characterized by a radial length, an azimuth angle and a vertical position. The 3D vectors (x, y, z) and (k_x, k_y, k_z) in Cartesian coordinates can be transformed to (r_i, θ_i, z_i) and (k_{ri}, ϕ_i, k_{zi}), $i \in \{g, 1, 2, s\}$, in cylindrical coordinates.

The dependence of 3D data for a 1D earth can be expressed as $D^{3D1DE}(|\vec{r_g} - \vec{r_s}|, \omega)$ or $D^{3D1DE}(r_h, \omega)$, where $\vec{r_g}$ and $\vec{r_s}$ are the projections of receiver and source locations on to the $x - y$ plane, respectively. Set $\vec{r_h} = \vec{r_g} - \vec{r_s}$ and r_h is the magnitude of the difference between $\vec{r_g}$ and $\vec{r_s}$. The Fourier transforms over 3D-source data become

$$\begin{aligned}
&D(\vec{k_g},\vec{k_s};\omega)\\
&=\iint\iint D^{3D1DE}(r_h,\omega)e^{i\vec{k_g}\vec{r_g}-i\vec{k_s}\vec{r_s}}d\vec{r_g}d\vec{r_s}\\
&=\iint\iint D^{3D1DE}(r_h,\omega)e^{i\vec{k_g}(\vec{r_g}-\vec{r_s})+i(\vec{k_g}-\vec{k_s})\vec{r_s}}d\vec{r_g}d\vec{r_s}\\
&=\underbrace{\iint D^{3D1DE}(r_h,\omega)e^{i\vec{k_g}\vec{r_h}}d\vec{r_g}}_{\text{part 1}}\underbrace{\iint e^{i(\vec{k_g}-\vec{k_s})\vec{r_s}}d\vec{r_s}}_{\text{part 2}}. \qquad (2.13)
\end{aligned}$$

Appendix A transforms integral variables from $\vec{r_g}$ to $\vec{r_h}$ for part 1 and appendix B solves the part 2 in equation (2.13). The equation (2.13) becomes,

$$D(\vec{k_g},\vec{k_s};\omega)=\iint D^{3D1DE}(r_h,\omega)e^{i\vec{k_g}\vec{r_h}}r_h dr_h d\theta_h(2\pi)^2\frac{\delta(k_{rg}-k_{rs})\delta(\phi_g-\phi_s)}{k_{rg}}. \qquad (2.14)$$

Due to the definition of a Hankel transform (expressed by a zero-order Bessel function of first kind J_0), the 3D source/1D subsurface data can be transformed to the (k_{ri},ω) domain as,

$$D(\vec{k_g},\vec{k_s};\omega)=D^{3D1DE}(k_{rh};\omega)(2\pi)^2\frac{\delta(k_{rg}-k_{rs})\delta(\phi_g-\phi_s)}{k_{rg}}, \qquad (2.15)$$

where

$$D^{3D1DE}(k_{rh};\omega)=2\pi\int_0^\infty D^{3D1DE}(r_h;\omega)J_0(k_{rh}r_h)r_h dr_h. \qquad (2.16)$$

Substitute the $D^{3D1DE}(r_h;\omega)$ by the deghosted data $D'^{3D1DE}(r_h;\omega)$ and change $D^{3D1DE}(k_{rh};\omega)$ to $D_1'^{3D1DE}(k_{rh};\omega)$ as a notation of free-surface multiple prediction input, and then equation (2.15) and (2.16) turns to be,

$$D(\vec{k_g},\vec{k_s};\omega)=D_1'^{3D1DE}(k_{rh};\omega)(2\pi)^2\frac{\delta(k_{rg}-k_{rs})\delta(\phi_g-\phi_s)}{k_{rg}}, \qquad (2.17)$$

where

$$D_1^{'3D1DE}(k_{rh};\omega) = 2\pi \int_0^{\infty} D^{'3D1DE}(r_h;\omega) J_0(k_{rh} r_h) r_h dr_h. \tag{2.18}$$

The form of data in the $(k_{ri};\omega)$ domain (equation (2.17)) contains the Dirac delta functions in cylindrical coordinates, which is equivalent to $\delta(k_{xg}-k_{xs})\delta(k_{yg}-k_{ys})$ in Cartesian coordinates.

Substituting equation (2.17) into the full 3D ISS FSME algorithm in equation (2.3) and then changing the variables of integration $dk_x dk_y$ to $k_r dk_r d\phi$ can produce,

$$\begin{aligned} & D_n^{'3D1DE}(k_{rg};\omega)(2\pi)^2 \frac{\delta(k_{rg}-k_{rs})\delta(\phi_g-\phi_s)}{k_{rg}} \\ = & \frac{1}{2i\pi^2\rho_r B(\omega)} \int_{-\infty}^{\infty}\int_{-\infty}^{\infty} k_r dk_r d\phi (2\pi)^2 \frac{\delta(k_{rg}-k_r)\delta(\phi_g-\phi)}{k_{rg}} D_1^{'3D1DE}(k_{rg};\omega) \\ & \times q(2\pi)^2 \frac{\delta(k_r-k_{rs})\delta(\phi-\phi_s)}{k_r} D_{n-1}^{'3D1DE}(k_r;\omega) e^{iq(\epsilon_g+\epsilon_s)}, \end{aligned} \tag{2.19}$$

where ϵ_g and ϵ_s are the depth of source and receivers, respectively. The lateral integrals $\iint k_r dk_r d\phi$ can be evaluated due to the Dirac delta functions. The equation (2.19) turns out to be,

$$\begin{aligned} & D_n^{'3D1DE}(k_{rg};\omega) \frac{\delta(k_{rg}-k_{rs})\delta(\phi_g-\phi_s)}{k_{rg}} \\ = & \frac{2}{i\rho_r B(\omega)} \frac{\delta(k_{rg}-k_{rs})\delta(\phi_g-\phi_s)}{k_{rg}} D_1^{'3D1DE}(k_{rg};\omega) q D_{n-1}^{'3D1DE}(k_{rs};\omega) e^{iq(\epsilon_g+\epsilon_s)}. \end{aligned} \tag{2.20}$$

Integrating over k_{rg} and ϕ_g on both sides gives the 3D source ISS FSME algorithm for 1D subsurface as,

$$D_n^{'3D1DE}(k_{rh};\omega) = \frac{2}{i\rho_r B(\omega)} D_1^{'3D1DE}(k_{rh};\omega) q D_{n-1}^{'3D1DE}(k_{rh};\omega) e^{iq(\epsilon_g+\epsilon_s)}, \tag{2.21}$$

for $n \geq 2$ and

$$D^{'3D1DE}(k_{rh};\omega) = \sum_{n=1}^{\infty} D_n^{'3D1DE}(k_{rh},\omega), \tag{2.22}$$

where $k_{rh} = k_{rg} = k_{rs}$ and $q = \mathrm{sgn}(\omega)\sqrt{(\omega/c_0)^2 - k_{rh}^2}$.

$D_n^{\prime 3D1DE}(k_{rh}, \omega)$ (n^{th}-order free-surface multiple prediction) or $D^{\prime 3D1DE}(k_{rh}, \omega)$ (free-surface multiple removed data) need to be transformed back to the space domain by an inverse Hankel transform (derived from two dimension Fourier transform due to the independence of the azimuth angle), instead of an inverse Fourier transform. The free-surface multiple prediction $D_n^{\prime 3D1DE}(r_h; \omega)$ can be obtained by using,

$$D_n^{\prime 3D1DE}(r_h; \omega) = \frac{1}{2\pi} \int_0^{\infty} D_n^{\prime 3D1DE}(k_{rh}; \omega) J_0(k_{rh} r_h) k_{rh} dk_{rh}. \tag{2.23}$$

Similarly, the free-surface multiple removed data can be transformed to the space-time domain by,

$$D^{\prime 3D1DE}(r_h; \omega) = \frac{1}{2\pi} \int_0^{\infty} D^{\prime 3D1DE}(k_{rh}; \omega) J_0(k_{rh} r_h) k_{rh} dk_{rh}. \tag{2.24}$$

In an acquisition geometry where sources and receivers are on the same streamer in a 3D survey, we can take r along any angle in the $x - y$ plane, including the specific choice of $r = x$.

2.4 Numerical tests

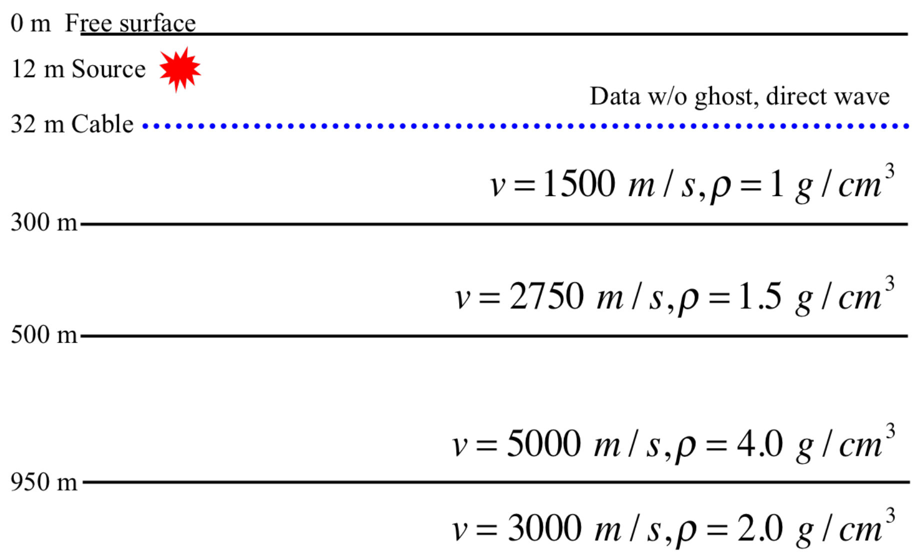

Figure 2.1: Three-reflector model with density-velocity variation for generating synthetic data. The depth of source, receivers, and reflectors are noted. Receiver internal is 4 m.

To show the significance of matching the source dimension in data and processing, a velocity-density varying model (Figure 2.1) is designed to synthesize 3D point source data. The synthetic 3D-source dataset (Figure 2.2) is a pre-stack shot gather without the reference wave and ghost, generated by reflectivity modeling method with a limited bandwidth. The synthetic data contain primaries, free-surface multiples, and internal multiples, where primaries and free-surface multiples dominate the energy of data. The free-surface multiples (up to 2^{rd} order) are the targets to be removed.

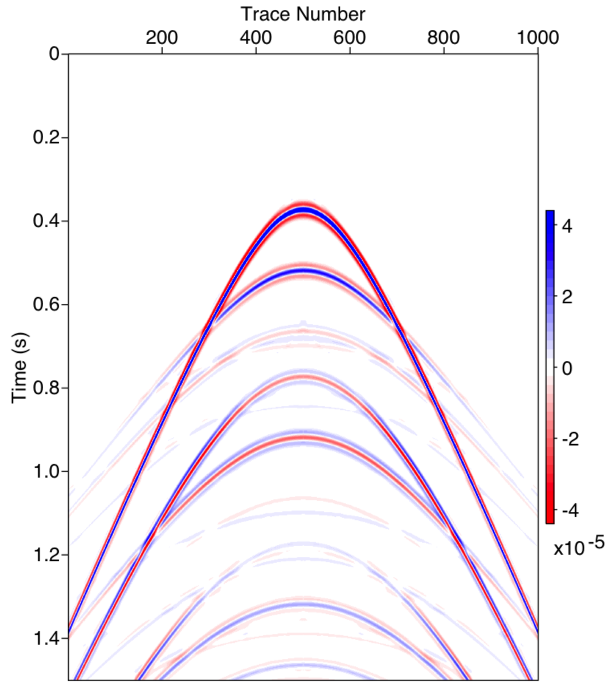

Figure 2.2: Synthetic 3D point source data for evaluating the difference between ISS free-surface multiple elimination assuming a 3D point source and a 2D line source. The color scale represents amplitude intensity.

Figure 2.3 presents the ISS free-surface multiple prediction results with different assumptions of source dimension. Please notice that the plot scales in Figure 2.3 (a) and (b) are different as shown in the highlighted red box at color bars. Shown with different color scales, both 2D line source and 3D point source free-surface multiple predictions provide distinct events in Figure 2.3. When the source dimension (3D point source) in processing matches the data, as seen in Figure 2.3 (a), the prediction result provides the accurate time and accurate amplitude of free-surface multiples, which can be plotted in the same scale as data ($-4 \sim 4 \times 10^{-5}$). However, the 2D line source prediction (Figure 2.3 (b)) produces a much less effective result. To make the 2D line source prediction result be visible, this plot applies a different color scale, which is 200 times smaller than actual data (red box, Figure 2.3 (b)).

In order to detect the difference between predicted and actual free-surface multiples, the comparison of trace plot is provided in Figure 2.4. The sample trace is extracted from 200 m offset. The top Figure in 2.4 compares input data (black line), ISS free-surface multiple predictions assuming a 2D line source (dash-dot blue line) and a 3D point source (dash red line). The 3D point source prediction (dash red line) agrees with actual data in both time and amplitude of free-surface multiples, which delivers the promise of ISS FSME algorithm. Subtracting this 3D-source prediction from input data can surgically remove the free-surface multiples as seen in Figure 2.5 (a).

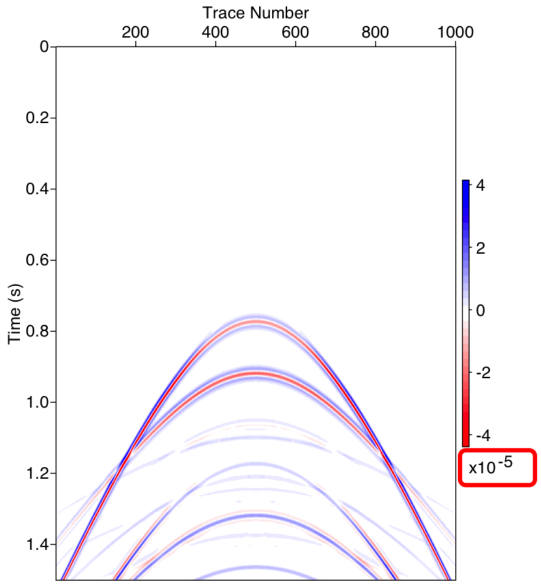

(a)

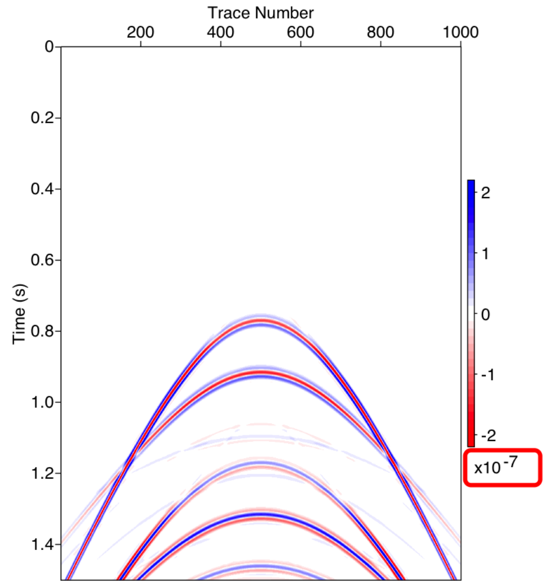

(b)

Figure 2.3: ISS free-surface multiple predictions assuming (a) a 3D point source versus (b) a 2D line source. The color scale represents amplitude intensity.

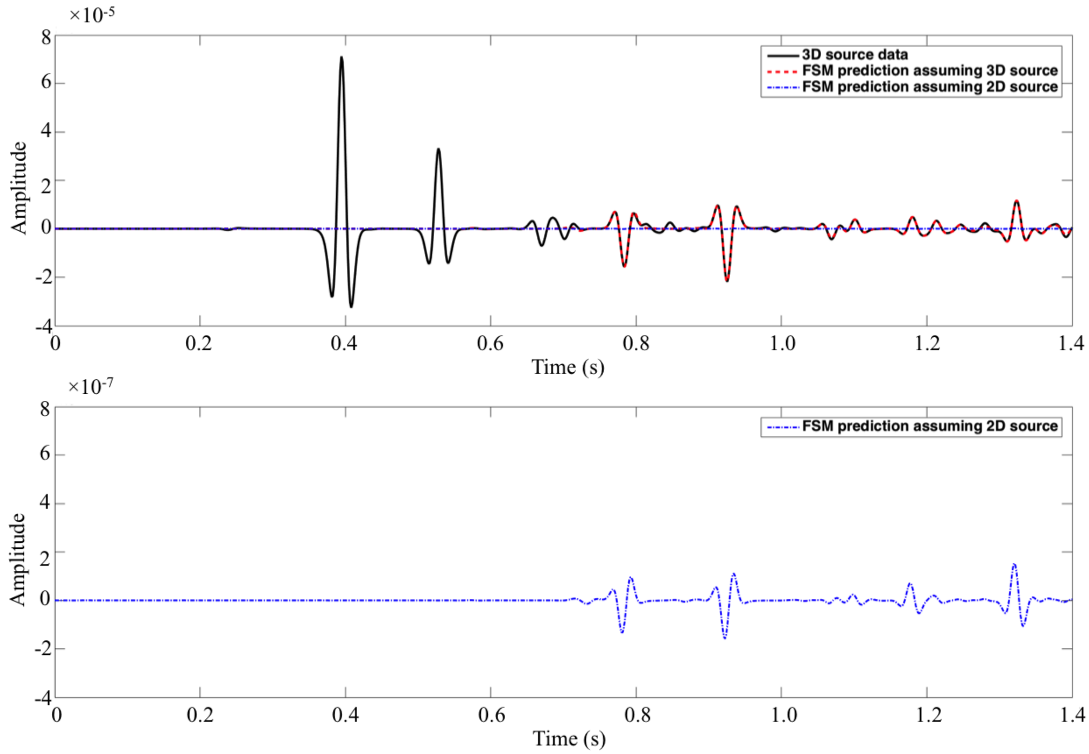

Figure 2.4: Top figure shows trace comparison at 200 m offset of input 3D point source data (solid black line), ISS free-surface multiple predictions assuming a 3D point source (dash red line) and a 2D line source (dash-dot blue line). Bottom figure replots the 2D line source prediction in top figure with a different scale.

In contract to 3D point source prediction, the 2D line source prediction (dash-dot blue line in Figure 2.4, top) shows a flat line because of the difference in amplitude scales. A visible plot of 2D line source prediction is provided at the bottom of Figure 2.4, which use a 100 times smaller amplitude scale than actual data. This replotted figure indicates that the mismatch of source dimension generates a significantly less effective result with deviated wavelet and small amplitude. In this case, subtracting the 2D line source prediction from the 3D point source data can produce serious free-surface multiple residues (Figure 2.5 (b)), which are harmful to subsequent processing (e.g. ISS internal multiple attenuation/elimination). Generally, the energy minimization criterion will be applied in this situation to make the subtraction effective, which is known as adaptive subtraction. And indeed, the adaptive subtraction works well when the events in the data are isolated. However, when the all the events are overlapping, the energy minimization criterion can fail to remove the multiples without harming the primaries.

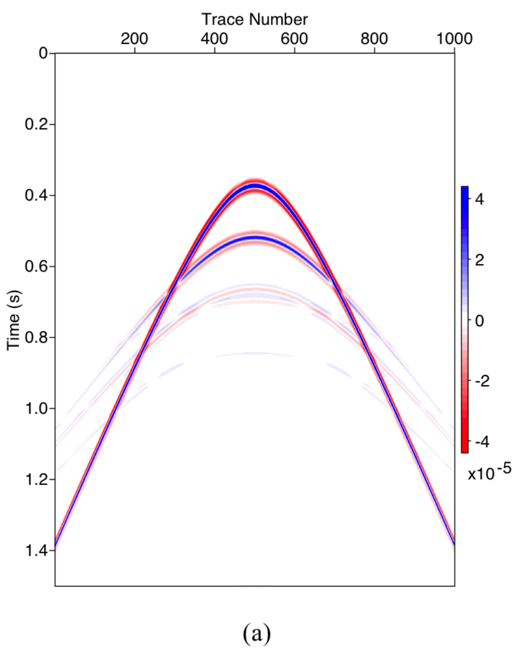

Figure 2.5: ISS free-surface multiple eliminated results assuming (a) a 3D point source versus (b) a 2D line source. The color scale represents amplitude intensity.

2.5 Analysis

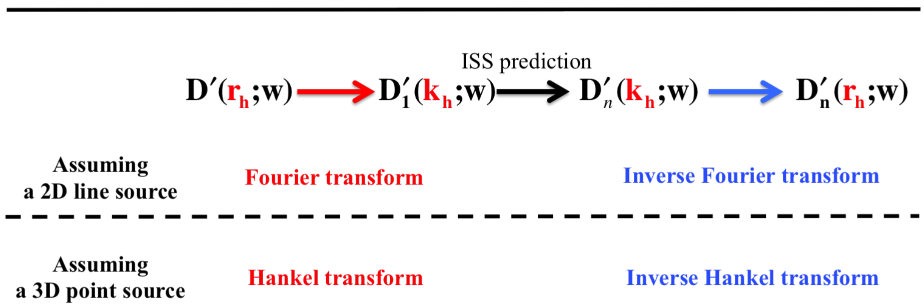

Figure 2.6: The essential difference between ISS free-surface multiple elimination algorithm assuming a 2D line source and a 3D point source in calculation.

To analyze the different results shown in previous section 2.4, Figure 2.6 illustrates the essential differences of calculations in 2D line source and 3D point source algorithms. Apparently, the differences between 2D line source algorithm and 3D point source algorithm are how to prepare input data in the wavenumber domain and how to transform the output back to the space domain. 2D line source algorithm requests a forward and an inverse Fourier transform. Instead, 3D point source algorithm needs a forward and an inverse Hankel transform. Meanwhile, the ISS free-surface multiple prediction kernel does not need to be altered.

The goal of analysis turns to clarify what is the difference between Fourier transform and Hankel transform and how this difference affects the ISS free-surface multiple prediction algorithm. In a 2D line source algorithm, the preparation of data requests a Fourier transform, which is

$$D^{2D1DE}(k_h;\omega) = \int D^{2D1DE}(x_h;\omega)e^{ik_hx_h}dx_h. \tag{2.25}$$

When data come from a 3D point source ($D^{3D1DE}(r_h;\omega)$) but processing depends on a 2D line source, the variable x_h in equation (2.25) can be changed to r_h (dummy variable), which produces

$$D^{2D}(k_{rh};\omega) = \int_{-\infty}^{+\infty} D(r_h;\omega) e^{ik_{rh}r_h} dr_h, \tag{2.26}$$

where the k_{rh} is the Fourier conjugate of r_h in the wavenumber domain. The superscript of data in the space domain is omitted since data are always coming from a 3D point source. In addition, on the left-hand side, the superscript of $2D1DE$ is changed to $2D$ to represent the source dimension carried by processing algorithm. Thereby, $D^{2D}(k_{rh};\omega)$ is the input of a 2D line source ISS free-surface multiple elimination algorithm.

Switch to a 3D point source algorithm. Preparing the input data needs a Hankel transform, which is

$$D^{3D}(k_{rh};\omega) = 2\pi \int_{0}^{+\infty} D(r_h;\omega) J_0(k_{rh}r_h) r_h dr_h, \tag{2.27}$$

where the superscript $3D$ represents the source dimension assumed by a processing algorithm. The Bessel function of first kind J_0 does not have a close form. In order to compare to a Fourier transform (applied in a 2D algorithm), two things need to happen: (1) rewriting a equivalent form of a Hankel transform with integral from $-\infty$ to $+\infty$, instead of 0 to $+\infty$; (2) explicitly writing out a form of the Bessel function with an asymptotic approximation. The rearranged formula of an asymptotic Hankel transform (appendix C) is,

$$D^{3D}(k_{rh};\omega) = \int_{-\infty}^{+\infty} D(r_h;\omega) \sqrt{\frac{2\pi r_h}{k_{rh}}} e^{ik_{rh}r_h - i\frac{\pi}{4}} dr_h. \tag{2.28}$$

Comparing equation (2.28) with (2.26), the asymptotic Hankel transform (equivalent to Hankel transform applied in a 3D point source algorithm for far-field) provides two factors which make it different from a Fourier transform. One is a $e^{-i\frac{\pi}{4}}$, which produces a phase change in the data. The other one is the factor $\sqrt{2\pi r_h/k_{rh}}$, which affects the amplitude of input. Reversely, when a 2D line source is assumed (where a Fourier transform is applied), the input preparation of data is lacking of these two factors. The input of a 2D line source algorithm carries one extra phase factor $e^{i\frac{\pi}{4}}$ (depending on the convention of the applied Fourier transform, appendix C) and one extra amplitude factor $\sqrt{k_{rh}/(2\pi r_h)}$, compared to the input of a 3D-source algorithm. Particularly, the amplitude in 2D line source input is $\sqrt{k_{rh}/(2\pi r_h)}$ times of 3D point source input, which can be estimated as a number < 1 with typical sampling parameters.

Continue to the ISS free-surface multiple prediction algorithm. Take the first-order free-surface multiple prediction as an example, which is quadratic in terms of input data. Namely, algorithm asks the multiplication of data to predict free-surface multiples. In this step, the phases of input are added and amplitudes of input are multiplied (by a rule that ISS method defines). Suppose that the 2D line source prediction is $D_2^{2D}(k_{rh};\omega)$ and the 3D point source prediction is $D_2^{3D}(k_{rh};\omega)$. Hence, the factors expected to be carried by $D_2^{2D}(k_{rh};\omega)$ are $e^{i\frac{\pi}{2}}$ and $k_{rh}/(2\pi r_h)$ compared to $D_2^{3D}(k_{rh};\omega)$. In higher order free-surface multiples prediction, the deviation on phase and decrease on amplitude in prediction can be more serious.

At the output step, different transforms have impact on predicted free-surface multiple events. Consistent with the convention in forward transforms, the inverse

Fourier transform (2D line source algorithm) and asymptotic inverse Hankel transform (3D point source algorithm) can be expressed as,

$$D_n^{2D}(r_h;\omega) = \frac{1}{2\pi}\int_{-\infty}^{+\infty} D_n^{2D}(k_{rh};\omega)e^{-ik_{rh}r_h}dk_{rh}, \tag{2.29}$$

and

$$D_n^{3D}(r_h;\omega) = \frac{1}{2\pi}\int_{-\infty}^{+\infty} D_n^{3D}(k_{rh};\omega)\sqrt{\frac{k_{rh}}{2\pi r_h}}e^{-ik_{rh}r_h+i\frac{\pi}{4}}dk_{rh}, \tag{2.30}$$

where D_n^{2D} and D_n^{3D} represent the ISS prediction result assuming a 2D line source and a 3D point source, respectively. Recall the example of the first-order free-surface multiple prediction. D_2^{3D} is transformed by adding two factors, $e^{i\frac{\pi}{4}}$ and $\sqrt{k_{rh}/(2\pi r_h)}$, which are missed in an inverse Fourier transform of D_2^{2D}. Eventually, all events in a 2D line source prediction $D_2^{2D}(r_h;\omega)$ are altered by $e^{i\frac{\pi}{4}}$ in phase and $\sqrt{k_{rh}/(2\pi r_h)}$ in amplitude compared to a 3D point source prediction that provides accurate time and amplitude of all free-surface multiples. And the small amplitude issue, which is shown in section 2.4, can be explained by the small number factor $\sqrt{k_{rh}/(2\pi r_h)}$. The $1/\sqrt{r_h}$ indicates that the negative impact of assuming a 2D line source varies along offset, which makes the adaptive subtraction even more difficult.

It is also worthwhile to point out that an asymptotic Hankel transform can adapt the Fast Fourier transform in numerical test, which is a way to reduce the cost of a real Hankel transform in computation when applying a 3D point source algorithm. However, the effectiveness of near offset can be sacrificed due to the far offset assumption in an asymptotic approximation.

2.6 Summary

In this chapter, a reduced and modified 3D point source ISS free-surface multiple elimination method is proposed for data coming from a 1D subsurface. The numerical results demonstrate that the reduced algorithm can successfully eliminate the free-surface multiples for one single 3D-source shot gather. The ignorance of 2D source dimension in the 1.5D algorithm can lead to dramatically decreased effectiveness of the ISS free-surface multiple prediction, which contains small amplitudes and distorted phases. Applying a 2D line source free-surface multiple prediction plus an adaptive subtraction can generate issues. When the events are interfering with each other, adaptive methods have difficulties in removing the multiples without harm to the primaries, whether a local search method (Verschuur et al., 1992) is used or a global search method (Carvalho and Weglein, 1994) is used. No matter what the earth dimension is 1D, 2D, or 3D, it is always important to incorporate a 3D-source dimension in processing, which is consistent of the real source dimension.

Chapter 3

Incorporating a 3D point source in ISS internal multiple attenuation (IMA) algorithm for a 1D/2D subsurface

This chapter firstly revisits the complete 2D and 3D ISS internal multiple attenuation algorithms. Secondly, based on these complete algorithms, it explains how to incorporate a 3D point source in ISS internal multiple prediction for a 1D/2D subsurface and shows the difference in internal multiple removal. The negative impact of mismatching the source dimension in free-surface multiple removal to the subsequent internal multiple prediction will be examined and analyzed. These results indicate that it is essential to accommodate a 3D point source in each step in seismic processing.

3.1 Introduction

The current state of ISS de-multiple algorithms provides a multidimensional procedure that attenuates all internal multiples (Araújo et al., 1994; Weglein et al., 1997, 2003). New ISS capabilities for internal multiple removal are pioneered by Liang et al. (2013); Zou and Weglein (2014); Ma and Weglein (2014). This approach has its unique strengths and does not require subsurface information. It is even independent of the earth model-type. Among these multidimensional methods, the ISS internal multiple attenuation algorithm (Araújo et al., 1994; Weglein et al., 1997) can predict the accurate time and approximate amplitude of internal multiple (that are downward reflected by the reflectors below the free-surface). Although ISS internal multiple removal does not require any subsurface information, it does care about the assumption of the source and earth dimensions. In history of developing 1D, 2D, and 3D algorithms, people have paid more attenuation to the earth dimensions, but ignored the source dimension. It is worthwhile to point out that a 2D algorithm is entirely 2D, including earth dimensions as well as the source dimension. When the the earth approximately varies in either 1D or 2D, the 2D algorithm is frequently used or reduced for a 1D earth. The reduced algorithm brings along the 2D source assumption, a line source in 3D sense. However, the source dimension in field data is actually a localized 3D point source, instead of a 2D line source. This discrepancy needs to be accommodated in the ISS de-multiple methods, including in free-surface multiple (chapter 2) and internal multiple removal, to deliver the promised effectiveness of de-multiple methods.

The implementations of ISS internal multiple attenuation have shown promising results for marine (e.g., Ferreira, 2011; Matson and Weglein, 1996) and onshore cases (e.g., Fu et al., 2010; Luo et al., 2011; Terenghi et al., 2011), with help of adaptive subtraction. There are circumstances where it is reasonable to assume a 1D subsurface (e.g., Central North sea, onshore Canada, and the Middle East). Recently, the 1.5D ISS internal multiple attenuator (2D line source/1D subsurface algorithm) has been successfully applied to Saudi Aramco onshore data (Luo et al., 2011) and also produced a positive result for the Encana land data (Fu and Weglein, 2014). Real data from a 2D subsurface have been tested by Ferreira (2011) using a complete 2D algorithm, which produces a positive internal multiple removed result. In these applications, people were aware that there was a danger of damaging interfering primaries by using an adaptive subtraction. Incorporating a more realistic 3D point source can improve the effectiveness of current internal multiple prediction, which benefits the reliability of simple subtraction and reduced the burden of adaptive subtraction.

This chapter presents how to incorporate a 3D point source in the ISS internal multiple attenuation to develop a more realistic algorithm for a 1D/2D subsurface. The significance of including a 3D source in the algorithm is numerically evaluated by synthetic 3D point source data. Moreover, the impact of an unsatisfactory free-surface multiple removal to the internal multiple prediction is exemplified and analyzed by numerical tests.

3.2 Review of complete 2D and 3D ISS internal multiple attenuation algorithms

The ISS internal multiple attenuator was originally proposed by Araújo et al. (1994) and Weglein et al. (1997), which provides a multi-dimensional approach for a 1D, 2D, and 3D world. The preparation of the 3D ISS internal multiple prediction starts from data $D(x_g, y_g, \epsilon_g, x_s, y_s, \epsilon_s; \omega)$, where (x_g, y_g, ϵ_g) and (x_s, y_s, ϵ_s) are the receiver- and source-location, respectively. For the fixed depth of sources and receivers (omit ϵ_s, ϵ_g), the b_1 term is defined by the data in wavenumber-frequency domain as $b_1(\vec{k}_g, \vec{k}_s; q_g + q_s) = -2iq_s D(\vec{k}_g, \vec{k}_s; \omega)$, where the vertical wavenumber is $q_i = \text{sgn}(\omega)\sqrt{(\omega/c_0)^2 - k_{x_i}^2 - k_{y_i}^2}$, $i \in \{g, s\}$ and $\vec{k_g} = (k_{x_g}, k_{y_g})$, $\vec{k_s} = (k_{x_s}, k_{y_s})$. The b_1 term can be Fourier transformed to the depth domain as $b_1(\vec{k}_g, \vec{k}_s; z)$, and corresponds to an un-collapsed Stolt migration. The ISS internal multiple attenuation algorithm in 3D is

$$
\begin{aligned}
& b_3^{3D}(k_{x_g}, k_{y_g}, k_{x_s}, k_{y_s}; \omega) \\
&= \frac{1}{(2\pi)^4} \iint dk_{x_1} dk_{x_2} \iint dk_{y_1} dk_{y_2} e^{-iq_1(\epsilon_g - \epsilon_s)} e^{iq_2(\epsilon_g - \epsilon_s)} \\
&\quad \times \int_{-\infty}^{+\infty} dz_1 b_1(k_{x_g}, k_{y_g}, k_{x_1}, k_{y_1}; z_1) e^{i(q_g + q_1) z_1} \\
&\quad \times \int_{-\infty}^{z_1 - \epsilon} dz_2 b_1(k_{x_1}, k_{y_1}, k_{x_2}, k_{y_2}; z_2) e^{-i(q_1 + q_2) z_2} \\
&\quad \times \int_{z_2 + \epsilon}^{+\infty} dz_3 b_1(k_{x_2}, k_{y_2}, k_{x_s}, k_{y_s}; z_2) e^{i(q_2 + q_s) z_3},
\end{aligned}
\tag{3.1}
$$

where the $q_i = \text{sgn}(\omega)\sqrt{(\omega/c_0)^2 - k_{x_i}^2 - k_{y_i}^2}$, $i \in \{g, 1, 2, s\}$, and b_3^{3D} is a 3D-internal-multiple attenuator in the wavenumber-frequency domain. The 3D algorithm in equation (3.1) assumes that the acquisition applies 3D sources and 3D receivers for a 3D subsurface. Inverse Fourier transforming $b_3^{3D}(k_{x_g}, k_{y_g}, k_{x_s}, k_{y_s}; \omega)/(-2iq_s)$ can produce the space-time domain attenuator. This attenuator predicts accurate time and approximate amplitude of all internal multiples at once. In addition, $(b_1 + b_3^{3D})/(-2iq_s)$ is the internal multiple removed 3D data when it returns to the space-time domain.

Similarly, a set of 2D data $D(x_g, x_s; t)$ can be transformed into wavenumber-frequency domain as $D(k_g, k_s; \omega)$, which defines the 2D $b_1(k_g, k_s, q_g + q_s) = -2iq_s \cdot D(k_g, k_s; \omega)$. And then the 2D ISS internal multiple attenuation algorithm is

$$
\begin{aligned}
& b_3^{2D}(k_g, k_s; \omega) \\
&= \frac{1}{(2\pi)^2} \iint dk_1 dk_2 e^{-iq_1(\epsilon_g - \epsilon_s)} e^{iq_2(\epsilon_g - \epsilon_s)} \\
&\times \int_{-\infty}^{+\infty} dz_1 b_1(k_g, k_1; z_1) e^{i(q_g + q_1) z_1} \\
&\times \int_{-\infty}^{z_1 - \epsilon} dz_2 b_1(k_1, k_2; z_2) e^{-i(q_1 + q_2) z_2} \\
&\times \int_{z_2 + \epsilon}^{+\infty} dz_3 b_1(k_2, k_s; z_2) e^{i(q_2 + q_s) z_3},
\end{aligned} \tag{3.2}
$$

where the vertical wavenumber is $q_i = \mathrm{sgn}(\omega)\sqrt{(\omega/c_0)^2 - k_i^2}$, $i \in \{g, 1, 2, s\}$, $b_1(k_g, k_s; z)$ is an un-collapsed Stolt migration of a 2D data (transform $b_1(k_g, k_s, q_g + q_s)$ back to depth domain), and $b_3^{2D}(k_g, k_s; \omega)$ is a 2D-internal-multiple attenuator in the wavenumber-frequency domain. The 2D attenuator in the space-time domain can be obtained by inverse Fourier transforming $b_3^{2D}(k_g, k_s; \omega)/(-2iq_s)$. In contrast to the 3D case, the algorithm in equation (3.2) assumes the acquisition corresponding to 2D line sources and 2D line receivers for a 2D subsurface.

3.3 Incorporating a 3D point source in ISS IMA for a 1D subsurface

In this section, the complete 3D ISS internal multiple attenuation algorithm is modified for a one-dimensional subsurface to improve realism and effectiveness. The new algorithm, which assumes that the earth only varies in the z-direction and the data carries along a 3D point source, represents more than a small increase in the effectiveness of predicting the amplitude of internal multiples, compared to a frequently employed 1.5D ISS internal multiple attenuator (assuming a 2D line source and a 1D earth). The difference of internal multiple prediction/removal assuming a 3D point source versus a 2D line source is exemplified by testing on synthetic 3D point source data, which matches the realistic source dimension in real data.

3.3.1 Theory

In the following sections, both the 3D and 2D internal multiple attenuation algorithms are reduced for the data coming from a 1D subsurface, where in the 3D case the source is a localized point source and in the 2D case the source is a line source. For convenience, the superscript $1DE$ represents the 1D earth assumption for different sources (For example, 2D line source 1D earth: $2D1DE$; 3D point source 1D earth: $3D1DE$).

3.3.1.1 Frequently used 2D line source/1D subsurface ISS IMA algorithm

In developing the algorithm for a 1D earth pre-stack data, it was natural that people started with the 2D ISS internal multiple attenuation algorithm and then reduced it for 1D-subsurface data. The data that occurs in the 2D earth can be represented as $D(x_g, x_s; \omega)$ or $D(x_m, x_h; \omega)$ in space-frequency domain, where $x_m = x_g + x_s$ and $x_h = x_g - x_s$. The data from a 1D earth, shown as $D^{2D1DE}(x_h; \omega)$, only depends on the source-receiver offset (x_h) and the frequency (ω). The Fourier transform over the 2D data for a 1D earth, which is needed for the algorithm, can be shown as,

$$\begin{aligned}
D(k_g, k_s; \omega) &= \iint e^{ik_g x_g} e^{-ik_s x_s} D^{2D1DE}(x_h; \omega) dx_g dx_s \\
&= \frac{1}{2} \int e^{ik_h x_h} D^{2D1DE}(x_h; \omega) dx_h \int e^{ik_m x_m} dx_m \\
&= D^{2D1DE}(k_h; \omega)(2\pi) \cdot \delta(k_g - k_s),
\end{aligned} \tag{3.3}$$

where $k_h = \frac{k_g + k_s}{2}$ and $k_m = \frac{k_g - k_s}{2}$. The data is independent of x_m and can come out of the integral. Consequently, the Fourier transform integral over x_m can produce a Dirac delta function in k_m. b_1 is defined as $b_1(k_g, k_s, q_g + q_s) = -2iq_s \cdot D(k_g, k_s; \omega)$. The uncollapsed Stolt migration b_1 can be expressed by b_1^{2D1DE} as,

$$b_1(k_g, k_s; z) = b_1^{2D1DE}(k_h; z)(2\pi) \cdot \delta(k_g - k_s). \tag{3.4}$$

By applying this 1D earth b_1 to the equation (3.2), the lateral integrals ($\int \int dk_1 dk_2$) can be evaluated by the Dirac delta functions. Then equation (3.2) produces the reduced 1.5D internal multiple attenuator as,

$$\begin{aligned} &b_3^{2D1DE}(k_h;\omega) = \\ &\int_{-\infty}^{+\infty} dz_1 b_1^{2D1DE}(k_h;z_1)e^{i2qz_1} \int_{-\infty}^{z_1-\epsilon} dz_2 b_1^{2D1DE}(k_h;z_2)e^{-i2qz_2} \\ &\times \int_{z_2+\epsilon}^{+\infty} dz_3 b_1^{2D1DE}(k_h;z_3)e^{i2qz_3}, \end{aligned} \tag{3.5}$$

where $k_h = k_g = k_s$ (evaluating by the Dirac delta functions) and $q = \mathrm{sgn}(\omega)\sqrt{(\omega/c_0)^2 - k_h^2}$. Prediction D_3 in the space domain can be obtained by an inverse Fourier transform as,

$$D_3^{2D1DE}(x_h;\omega) = \frac{1}{2\pi}\int b_3^{2D1DE}(k_h;\omega)/(-2iq_s)e^{ik_hx_h}dk_h. \tag{3.6}$$

The process following equation (3.5) and (3.6) provides the ISS internal multiple attenuation algorithm assuming a 2D line source for a 1D subsurface.

3.3.1.2 Reduced 3D point source/1D subsurface ISS IMA algorithm

The 3D data generated by a 1D earth only depends on the source-receiver offset and the frequency, which has a spatial circular symmetry in cylindrical coordinates (independence of azimuth angle). This symmetry makes it convenient to study the 1D earth problem with cylindrical coordinates. The 3D vectors (x, y, z) and (k_x, k_y, k_z) in Cartesian coordinates can be transformed to (r_i, θ_i, z_i) and (k_{ri}, ϕ_i, k_{zi}), $i \in \{g, 1, 2, s\}$, in cylindrical coordinates, which is characterized by a radial length, an azimuth angle and a vertical position.

The dependence of 3D data for a 1D earth can be expressed as $D^{3D1DE}(|\vec{r_g} - \vec{r_s}|;\omega)$ or $D^{3D1DE}(r_h;\omega)$, where the $\vec{r_g}$ and $\vec{r_s}$ are the projection of receiver and source locations on $x-y$ plane, respectively. By defining $\vec{r_h} = \vec{r_g} - \vec{r_s}$, r_h is the magnitude of the difference between $\vec{r_g}$ and $\vec{r_s}$. Due to the cylindrical symmetry, the 3D source/1D subsurface data can be transformed to $(k_{ri};\omega)$ domain as,

$$D(\vec{k_g},\vec{k_s};\omega) = D^{3D1DE}(k_{rh};\omega)(2\pi)^2\frac{\delta(k_{rg}-k_{rs})\delta(\phi_g-\phi_s)}{k_{rg}}, \tag{3.7}$$

where $k_{rh} = k_{rg}$. The receivers are required along the r-direction as $D^{3D1DE}(r_h;\omega)$, because

$$D^{3D1DE}(k_{rh};\omega) = 2\pi\int_0^\infty D^{3D1DE}(r_h;\omega)J_0(k_{rh}r_h)r_h dr_h. \tag{3.8}$$

The 3D-source data in $(k_{ri};\omega)$ domain (equation (3.7)) contain the Dirac delta functions in cylindrical coordinates, which is equivalent to $\delta(k_{x_g}-k_{x_s})\delta(k_{y_g}-k_{y_s})$ in Cartesian coordinates. Preparing input b_1 uses,

$$b_1(\vec{k_g},\vec{k_s};z) = b_1^{3D1DE}(k_{rg};z)(2\pi)^2\frac{\delta(k_{rg}-k_{rs})\delta(\phi_g-\phi_s)}{k_{rg}}, \tag{3.9}$$

which is a 3D uncollapsed Stolt migration with water-speed. Substitute formula (3.9) into the full 3D ISS internal multiple attenuation algorithm in equation (3.1) with arranging the integral variable from $dk_x dk_y$ to $k_r dk_r d\phi$ as,

$$\begin{aligned}
& b_3^{3D1DE}\cdot\frac{\delta(k_{rg}-k_{rs})\delta(\phi_g-\phi_s)}{k_{rg}} \\
= & \int_0^\infty k_{r1}dk_{r1}\int_0^{2\pi}d\phi_1\int_0^\infty k_{r2}dk_{r2}\int_0^{2\pi}d\phi_2 \\
& \times\int_{-\infty}^{+\infty}dz_1 b_1^{3D1DE}(k_{rg};z_1)e^{i(q_g+q_1)z_1}\frac{\delta(k_{rg}-k_{r1})\delta(\phi_g-\phi_1)}{k_{rg}} \\
& \times\int_{-\infty}^{z_1-\epsilon}dz_2 b_1^{3D1DE}(k_{r1};z_2)e^{-i(q_1+q_2)z_2}\frac{\delta(k_{r1}-k_{r2})\delta(\phi_1-\phi_2)}{k_{r1}} \\
& \times\int_{z_2+\epsilon}^{+\infty}dz_3 b_1^{3D1DE}(k_{r2};z_3)e^{i(q_2+q_s)z_3}\frac{\delta(k_{r2}-k_{rs})\delta(\phi_2-\phi_s)}{k_{r2}}.
\end{aligned} \tag{3.10}$$

The lateral integrals $\iiiint k_{r1}dk_{r1}d\phi_1 k_{r2}dk_{r2}d\phi_2$ can be evaluated due to the Dirac delta functions in equation (3.7). The reduced form of the 3D algorithm is

$$\begin{aligned} & b_3^{3D1DE}(k_{rh};\omega) = \\ & \int_{-\infty}^{+\infty} dz_1 b_1^{3D1DE}(k_{rh};z_1)e^{i2qz_1} \int_{-\infty}^{z_1-\epsilon} dz_2 b_1^{3D1DE}(k_{rh};z_2)e^{-i2qz_2} \\ & \times \int_{z_2+\epsilon}^{+\infty} dz_3 b_1^{3D1DE}(k_{rh};z_3)e^{i2qz_3}, \end{aligned} \tag{3.11}$$

where $k_{rh} = k_{rg} = k_{rs}$ (evaluated by Dirac delta functions), vertical wavenumber $q = \mathrm{sgn}(\omega)\sqrt{(\omega/c_0)^2 - k_{rh}^2}$ and $\epsilon_g = \epsilon_s$. Equation (3.11) has the same form as the 1.5D internal multiple attenuator (equation (3.5)) in the wavenumber-frequency domain, which indicates that the prediction kernel does not change in different source-dimension assumptions.

$b_3^{3D1DE}(k_{rh};\omega)$ needs to be transformed back to the space domain by an inverse Hankel transform (derived from two dimension Fourier transform due to the independence of the azimuth angle), instead of an inverse Fourier transform. The internal multiple prediction $D_3^{3D1DE}(r_h;\omega)$ can be obtained by using,

$$D_3^{3D1DE}(r_h;\omega) = \frac{1}{2\pi}\int_0^{\infty} J_0(k_{rh}\cdot r_h)\frac{b_3^{3D1DE}(k_{rh};\omega)}{-2iq_s}k_{rh}dk_{rh}. \tag{3.12}$$

In a specified acquisition geometry that sources and receivers are on the same streamer in a 3D survey, we can make r along any angle in $x-y$ plane, including $r = x$. The equations (3.11), (3.8), and (3.12) forms the ISS internal multiple attenuator assuming a 3D point source for 1D subsurface.

3.3.2 Numerical tests

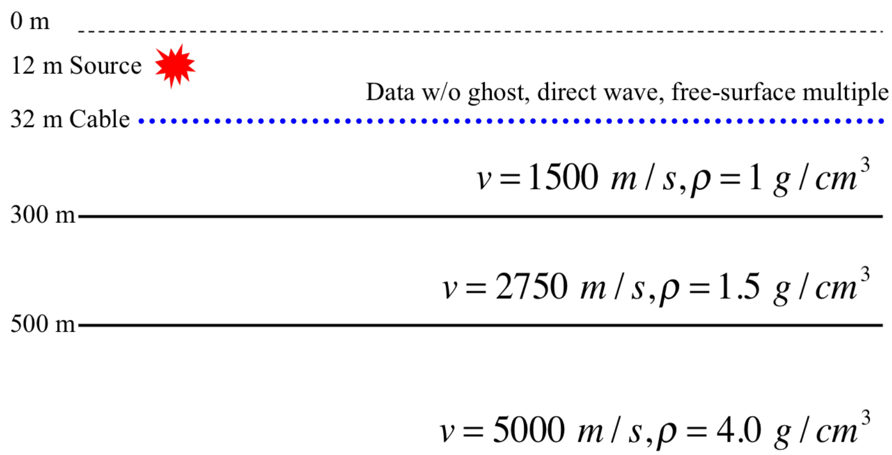

Figure 3.1: Two-reflector model with velocity-density variation for generating synthetic data. The depths of source, receivers, and reflector locations are noted. Receiver intervel is 4 m.

To show the significance of matching the source dimension in ISS internal multiple attenuation algorithm and actual data, a two-reflector model (Figure 3.1) is designed to synthesize 3D point source data (Figure 3.2), without the reference wave, ghost and free-surface multiple. The forward modeling employs a reflectivity method with limited bandwidth. The data contains primaries and internal multiples in different orders. In following test, only the first-order internal multiple is the target, which is supposed to be attenuated in principle.

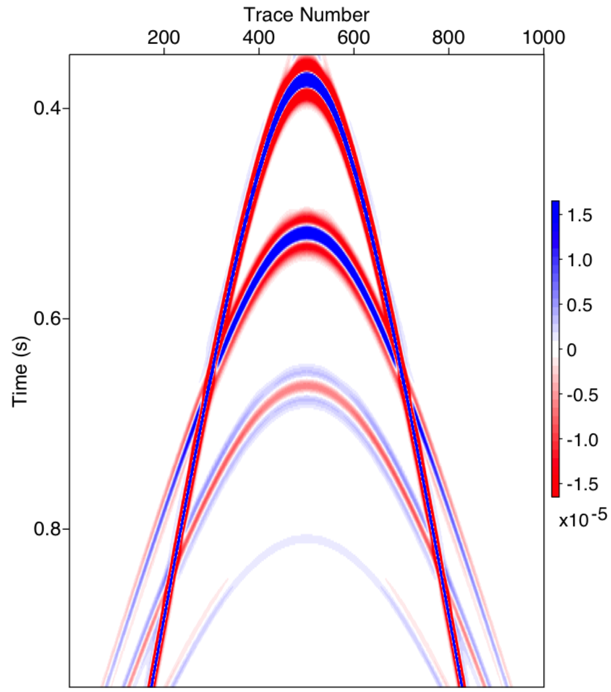

Figure 3.2: Synthetic 3D point source data for evaluating the difference between ISS internal multiple attenuation assuming a 3D point source and a 2D line source. The color scale represents amplitude intensity.

The ISS internal multiple prediction results with different assumptions of source dimension are presented in Figure 3.3. Both results were able to predict internal multiple events, but the effectiveness in these two results were different. The 3D point source internal multiple prediction (Figure 3.3 (a)) provides an accurate time and approximate amplitude for internal multiples, which delivered the promise of an ISS internal multiple attenuation algorithm. However, the 2D line source prediction (Figure 3.3 (b)) produced a much less effective result due to the mismatch of the source dimension. To make the 2D line source prediction visible, the plot of Figure 3.3 (b) applies a significantly small color scale ($10^4 \sim 10^5$ times smaller than data), which indicates that the amplitude difference is greater than the amplitude difference in a mismatched free-surface multiple prediction can produce (chapter 2, section 2.4). The difference between the amplitude intensity of 3D point source and 2D line source prediction is highlighted by red boxes seen in Figure 3.3.

To further study this difference, the trace at 200 m offset is extracted from the input 3D point source data (Figure 3.2), a 2D line source IMA prediction (Figure 3.3 (a)) and a 3D point source IMA prediction (Figure 3.3 (b)). The comparison of these three traces is shown on the top part of Figure 3.4. The first-order internal multiple event is an isolated event (at 0.68s). By tracking this event, the 3D point source prediction (solid red line) provides accurate phase and approximate amplitude of this event. The approximate amplitude is still in the same scale of input data, which allows the internal multiple attenuation through a simple subtraction between data (Figure 3.2) and 3D point source prediction (Figure 3.3 (a)). The attenuated result after subtraction is shown in Figure 3.5 (a), in which the energy of internal multiples is effectively suppressed.

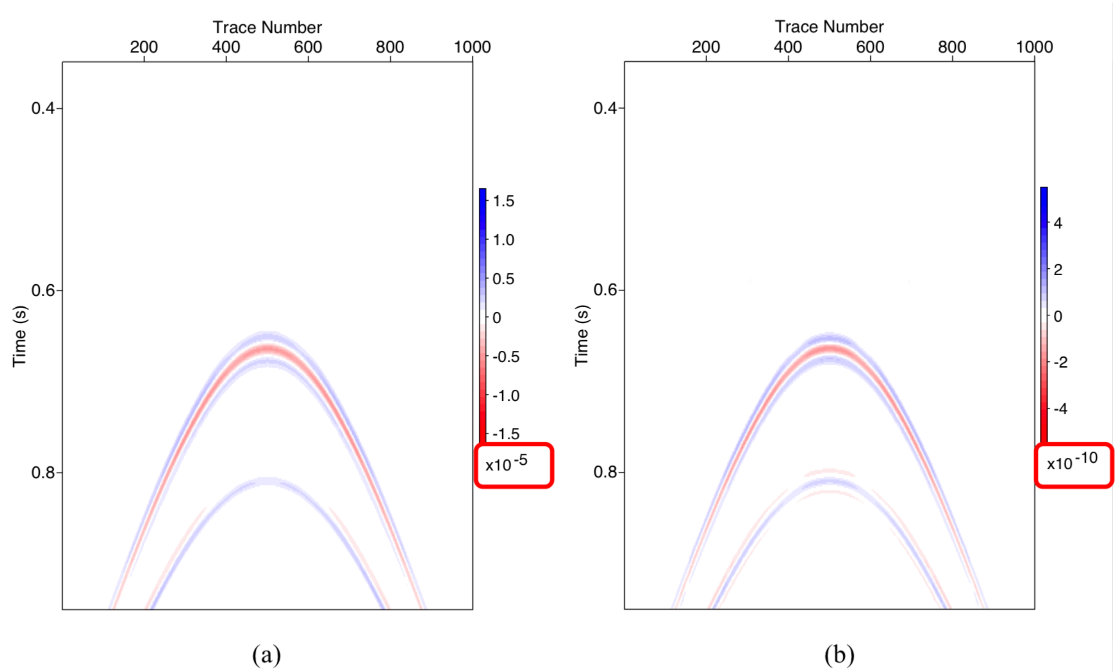

Figure 3.3: ISS internal multiple predictions assuming (a) a 3D point source versus (b) a 2D line source. The color scale represents amplitude intensity.

The 2D line source prediction (dash-dot blue line in Figure 3.4) shows a flat line because of a less effective prediction. A visible trace of 2D line source prediction (dash-dot blue line) is replotted at the bottom of Figure 3.4 with a new scale ($-4 \sim 8 \times 10^{-10}$). In other words, the internal multiples predicted by 2D line source algorithm is about $10^4 \sim 10^5$ times smaller than actual 3D point source internal multiples in amplitude. A change of phase is not observed in the 2D line source internal multiple prediction, which will be discussed in section 3.3.3. Subtracting this prediction from the 3D point source data cannot help the removal or attenuation of internal multiples. Figure 3.5 (b) gives the result after subtracting the 2D line source internal multiple prediction from 3D point source data. There is few change of internal multiple energy, especially compared to the 3D point source internal multiple attenuated result in Figure 3.5 (a).

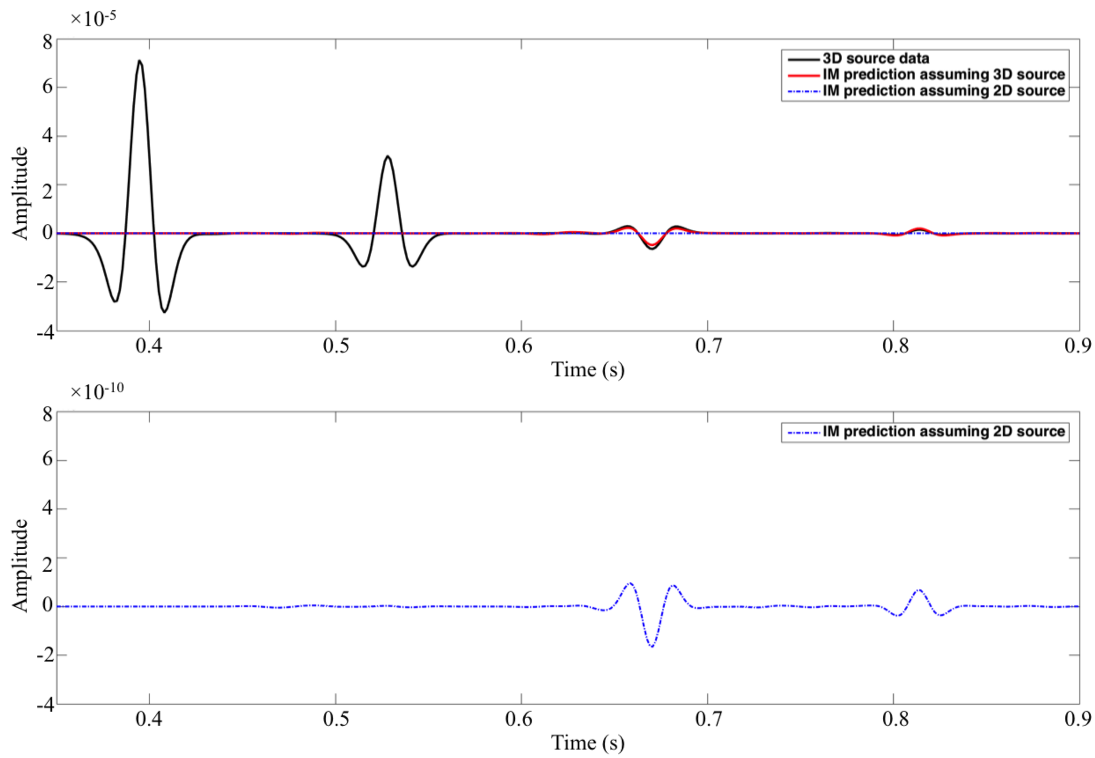

Figure 3.4: Top figure shows trace comparison at 200 m offset of input 3D point source data (solid black line), ISS internal multiple predictions assuming a 3D point source (solid red line) and a 2D line source (dash blue line). Bottom figure replots the 2D line source prediction in top figure with a different scale.

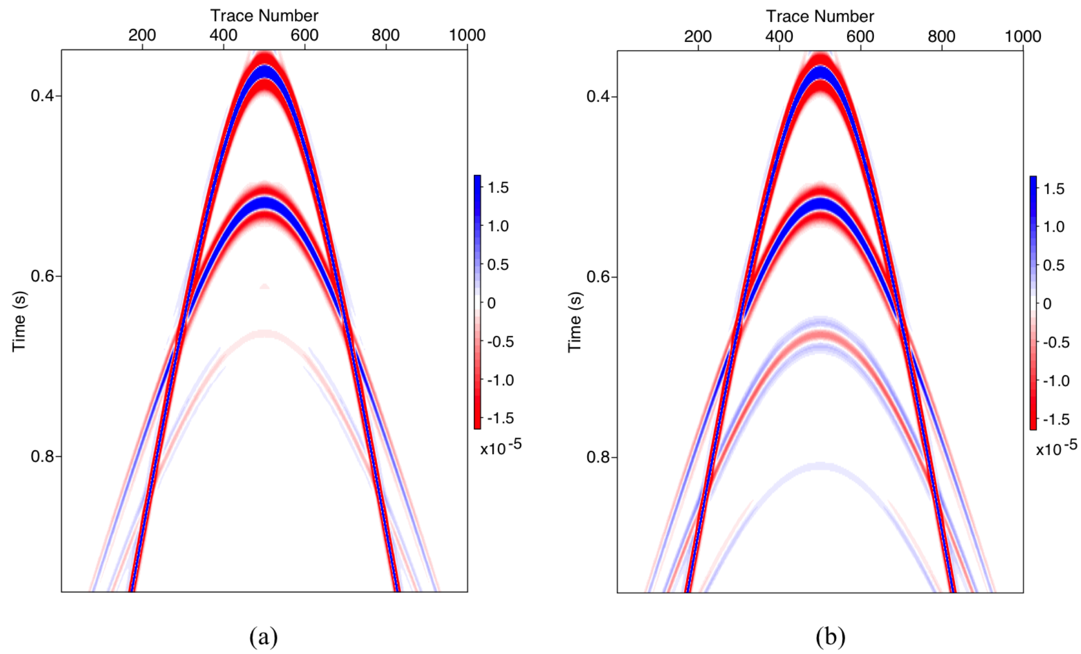

Figure 3.5: ISS internal multiple attenuated results assuming (a) a 3D point source versus (b) a 2D line source. The color scale represents amplitude intensity.

3.3.3 Analysis

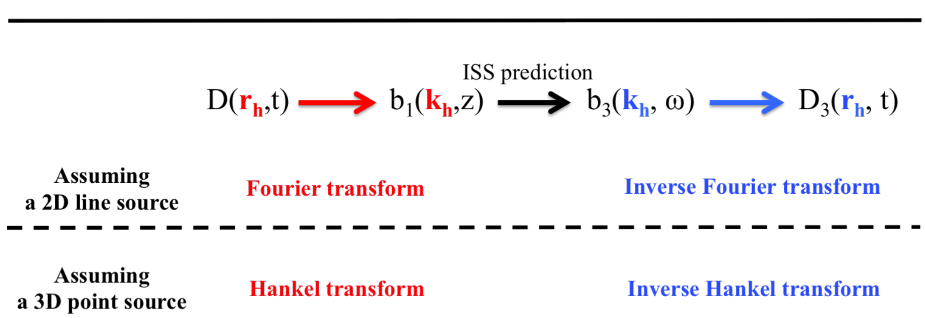

Figure 3.6: The essential difference between ISS internal multiple attenuation algorithm assuming a 2D line source and a 3D point source in calculation.

Figure 3.6 illustrates the essential difference of how to implement 2D line source and 3D point source ISS internal multiple prediction algorithms, in order to analyze the numerical results of internal multiple predictions seen in section 3.3.2. Similar to free-surface multiple prediction, the difference between 2D line source and 3D point source internal multiple predictions are how to prepare input data in the wavenumber domain and how to transform the output back to the space domain. In general, internal multiple prediction utilizes transformed data to prepare b_1 as input, which is a water-speed migration. After predicting internal multiples in b_3, ISS algorithm applies a transform on b_3 to output internal multiple prediction in the space domain. The 2D line source algorithm requests a forward and an inverse Fourier transform. Instead, the 3D point source algorithm requires a forward and an inverse Hankel transform. Meanwhile, the ISS internal multiple prediction kernel is not altered.

The difference between a Fourier transform and an asymptotic Hankel transform can be shown by two classes of factors, discussed section 2.5. One is a $e^{-i\frac{\pi}{4}}$, that produces a phase change. The other one is the factor $\sqrt{2\pi r_h/k_{rh}}$, which affects the amplitude of the input and output. Reversely, input of 2D line source carries one more phase factor $e^{i\frac{\pi}{4}}$ and one more amplitude factor $\sqrt{k_{rh}/(2\pi r_h)}$. Particularly, the amplitude in 2D line source input is $\sqrt{k_{rh}/(2\pi r_h)}$ times the 3D point source input. This can be estimated as a number < 1 with typical sampling parameters.

ISS internal multiple multiple prediction algorithm is extracted/selected from the subseries higher than third-order in inverse scattering series. In the first-order internal multiple prediction $b_3(k_h;\omega)$ (extracted from the third-order subseries), prediction demands the cubic multiplication of migrated data $b_1(k_h;z)$. Fortunately,

$b_1(k_h; z)$ is linear. With three migrated $b_1(k_h; z)$s, the algorithm adds the phase from two outer $b_1(k_h; z)$s and subtracts the phase from the middle $b_1(k_h; z)$. If the algorithm assumes a 2D line source, the phase factor $e^{-i\frac{\pi}{4}}$ is canceled by adding the phase of two b_1s and subtracting the phase of one b_1. Only one $e^{i\frac{\pi}{4}}$ is left in $b_3(k_h; \omega)$. Also, the algorithm multiplies the amplitude in each b_1, so the amplitude factor is multiplied three times. Consequently, $b_3(k_h; \omega)$ with a 2D line source assumption carries a factor $(k_{rh}/(2\pi r_h))^{3/2}$ in amplitude.

When the 2D line source internal multiple prediction is transformed into the space domain, the difference of inverse Fourier and Hankel transform produces factors in a reverse of forward transforms. If a 2D line source is assumed in the algorithm, there will be no phase change in the final internal multiple prediction in the space-time domain, but the amplitude of predicted internal multiples can be altered by an extremely small factor $k_{rh}/(2\pi r_h)$. That is the reason why mismatching the source dimension and ISS internal multiple attenuation can produce a significantly less-effective result, especially for amplitude prediction.

3.4 Negative consequence of mismatching the source dimension in the ISS FSME to the ISS IMA

This section aims to examine the consequence of mismatching the source dimension in free-surface multiple removal to the subsequent internal multiple prediction. Completely removing free-surface multiples in data is a prerequisite for ISS internal multiple prediction. For 3D point source data coming from a 1D subsurface, the effective free-surface removal assuming a 3D point source can be obtained by applying equation (2.22) and (2.24) in section 2.3.2. However, a 1.5D free-surface multiple removal for 3D-source data leads to serious free-surface multiple residues, which becomes sub-events in b_1. The influence of these free-surface multiple residues in a 3D point source internal multiple prediction is illustrated by a numerical example.

3.4.1 Numercial tests

This test was performed on the data generated by a 3D point source and a density-variable model (Figure 3.7) using a reflectivity method. The original data seen in Figure 3.8 contain two primaries, three free-surface multiples and one internal multiple. Since the data contains both first-order and second-order free-surface multiples, the second-order ISS FSME algorithm was applied to eliminate the free-surface multiples in the original data.

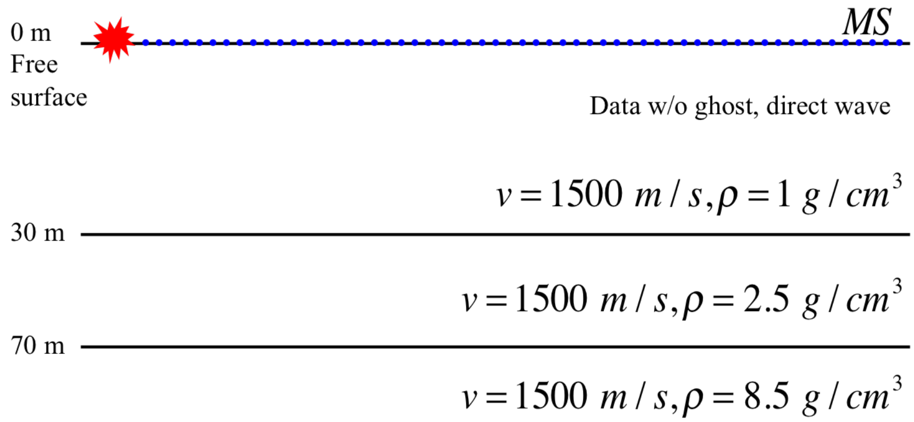

Figure 3.7: The synthetic model for the numerical test.

Figure 3.9 (a) presents the free-surface multiple removed result assuming a 3D point source, which matches the source dimension in the synthetic data. Incorporating the 3D source can provide both the accurate time and amplitude for this 3D point source dataset. Therefore, all the free-surface multiples can be removed. The result is seen in Figure 3.9 (a) produces the satisfactory prerequisite of subsequent ISS internal multiple attenuation algorithm. Continued ISS internal multiple attenuation prediction is seen in the right panel of Figure 3.9 (b). The yellow arrow is pointed to the predicted internal multiple event. The internal multiple attenuation prediction works well as an attenuator, which provides accurate time and approximate amplitude of the internal multiple event.

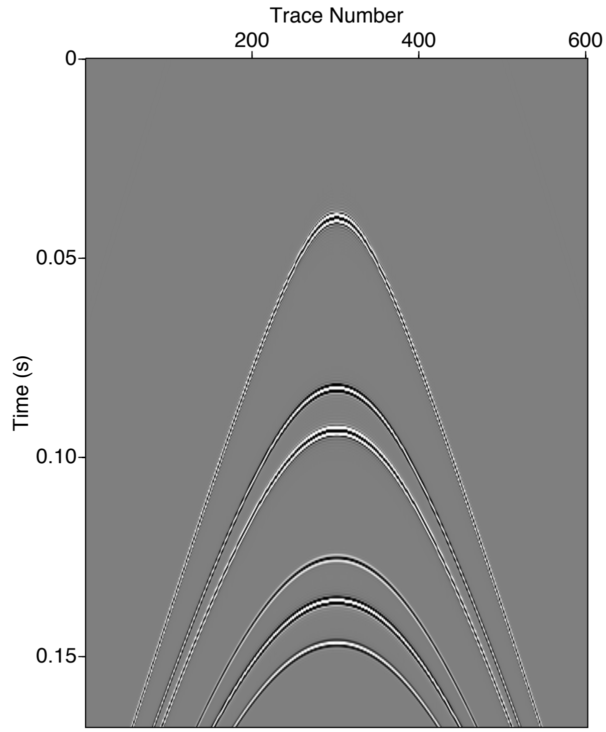

Figure 3.8: The synthetic data generated by the model seen in Figure 3.7 for the numerical test.

However, applying a frequently used 2D line source FSME algorithm on a 3D point source data can produce an ineffective free-surface multiple prediction. The free-surface multiple removal assuming a 2D line source is seen in Figure 3.10 (a). Compared to the original data seen in Figure 3.8, the free-surface multiple residues present in the result after free-surface multiple removal. If the residues of free-surface multiples exist in the input of subsequent ISS internal multiple attenuation, several artifacts occur in the internal multiple prediction. Figure 3.10 (b) shows the source-dimension-mismatched FSME prediction in the left panel and the internal multiple prediction using the left panel result as input in the right panel. The artifacts (right panel of Figure 3.10 (b)) are cataloged as (1) false events (green arrows), (2) events sitting on the free-surface multiple residues (red arrows), and (3) events sitting on the internal multiple prediction (yellow arrow).

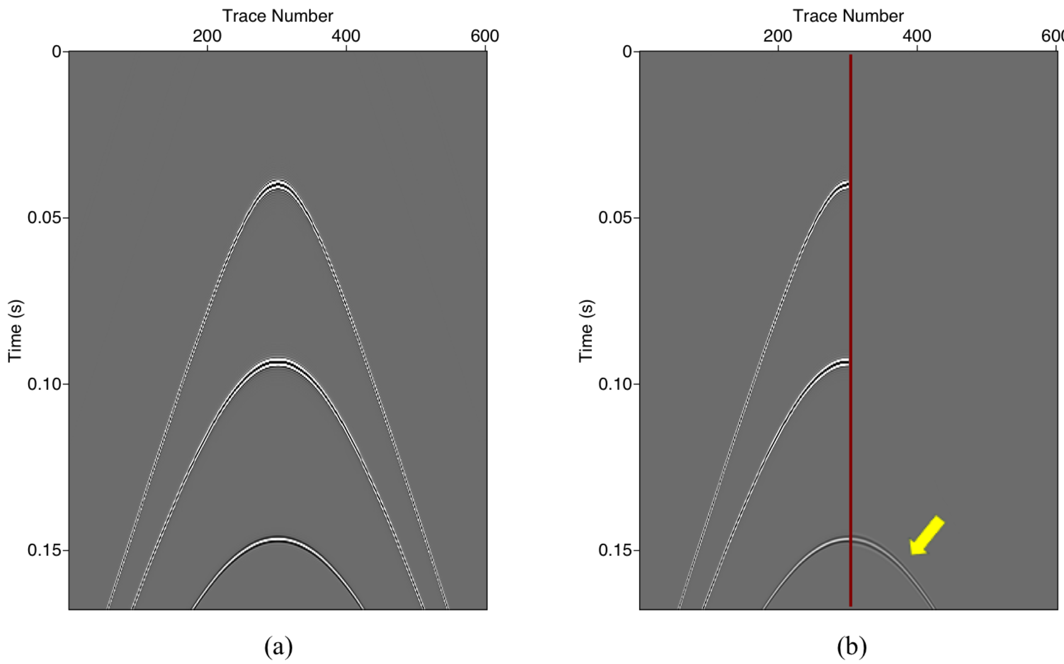

Figure 3.9: (a) ISS free-surface multiple removal result assuming a 3D point source and (b) comparison between 3D point source FSME result (left panel) and continued 3D point source ISS internal multiple attenuation prediction (right panel) using the result in (a) as input. Yellow arrow indicates the internal multiple prediction.

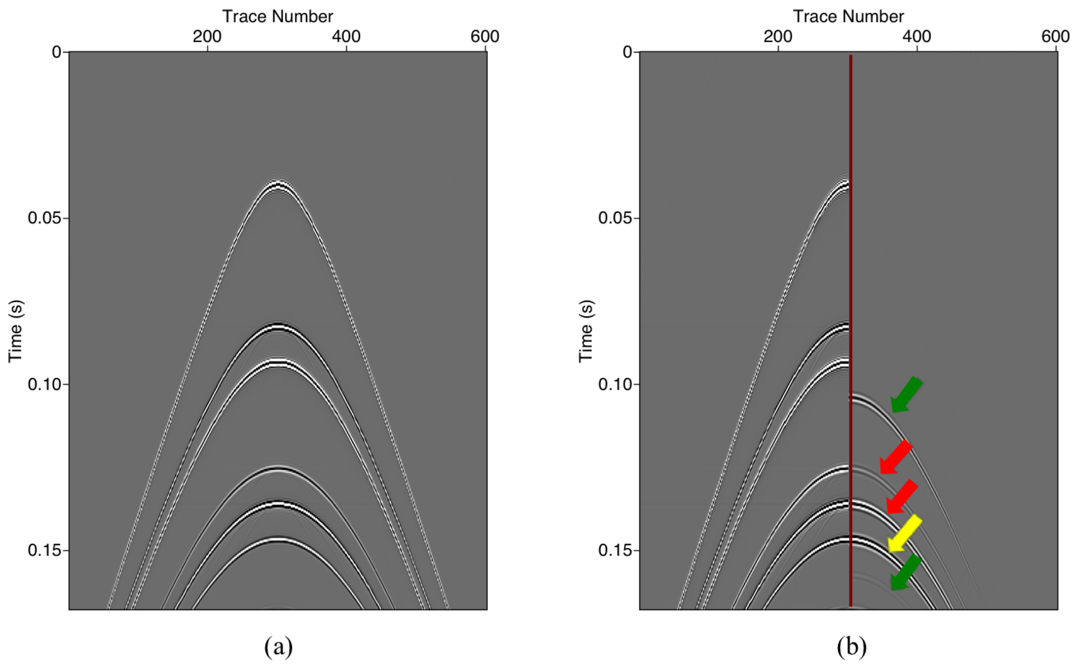

Figure 3.10: (a) ISS free-surface multiple removal result assuming a 2D line source and (b) comparison between 2D line source FSME result (left panel) and a continued 3D point source ISS internal multiple attenuation prediction (right panel) using the result in (a) as input. Green arrow shows false events. Red arrow shows events on the FSM residue. Yellow arrow shows events on the internal multiple prediction.

3.4.2 Analysis

The causes of different artifacts are presented in Figure 3.11, 3.12, and 3.13 with ray-path plots. The internal multiple attenuation algorithm selects events, which satisfy the lower-higher-lower relation of vertical time in input b_1. Summing over the time in two b_1s (denoted by blue font in Figure 3.11, 3.12, and 3.13) and then subtracting the time in middle b_1 (denoted by red font in Figure 3.11, 3.12, and 3.13) can produce an accurate phase of internal multiples.

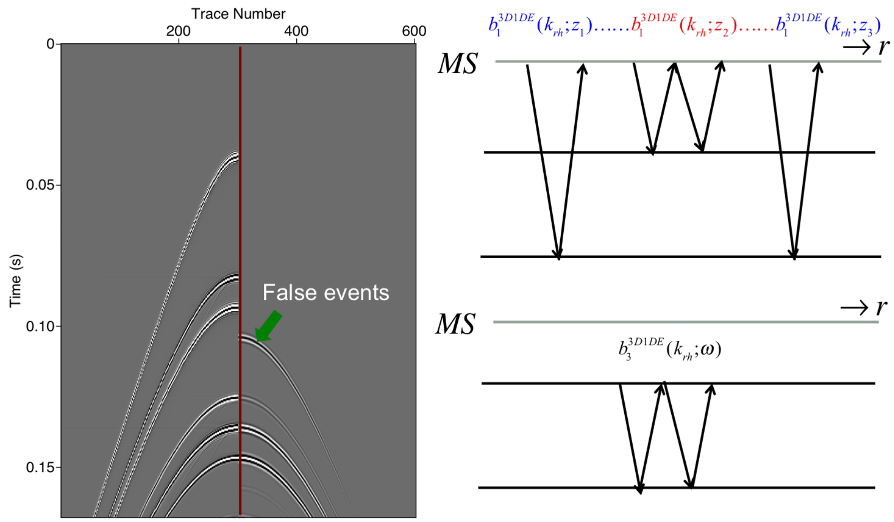

Figure 3.11: The analysis of the false events generated by ISS internal multiple prediction using the input that contains free-surface multiple residues.

Figure 3.11 shows the origin of false events (green arrow) that do not exist in the original data. Generally, false events can occur when the outer b_1s contribute primaries arriving at long times and the middle b_1 contributes to a free-surface multiple event arriving at a short time.

Figure 3.12 shows the second type of artifact (red arrow), sitting on the free-surface multiple residues in time. This artifact always exists as long as the free-surface multiple cannot be completely removed before internal multiple prediction. After subtracting this internal multiple prediction (right panel) from the input (left panel), this artifact can make the free-surface multiples residues worse.

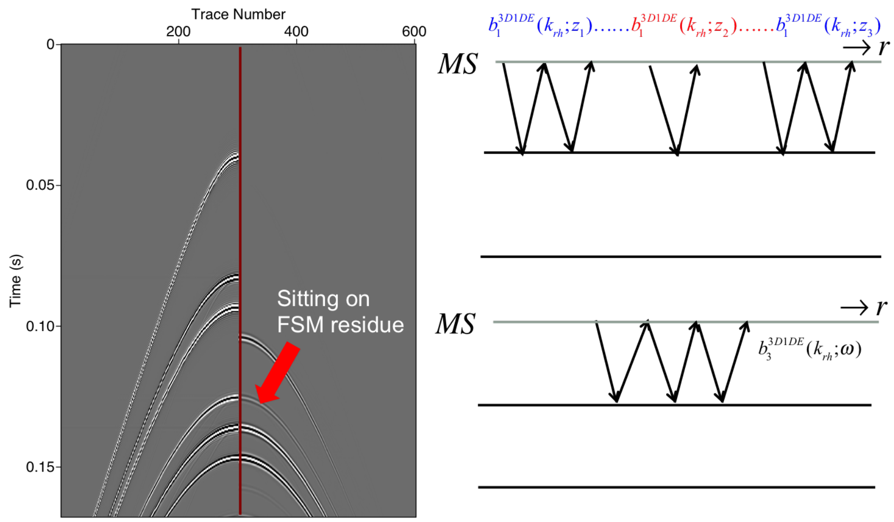

Figure 3.12: The analysis of the events sitting on the free-surface multiple residues generated by ISS internal multiple prediction using the input that contains free-surface multiple residues.

The third kind of artifact, sitting on the internal multiple prediction as seen in Figure 3.13, has the possibility to destroy the internal multiple attenuation. The way to predict the internal multiple ray-path seen in Figure 3.13 is not supposed to happen. Nevertheless, if the input data contain free-surface multiple residues, this combination (which produces the same phase as actual internal multiple) can happen and it can enlarge the amplitude of the internal multiple prediction. In this case, the attenuation of internal multiples can fail when the amplitude of the prediction is higher than the amplitude of the original internal multiple.

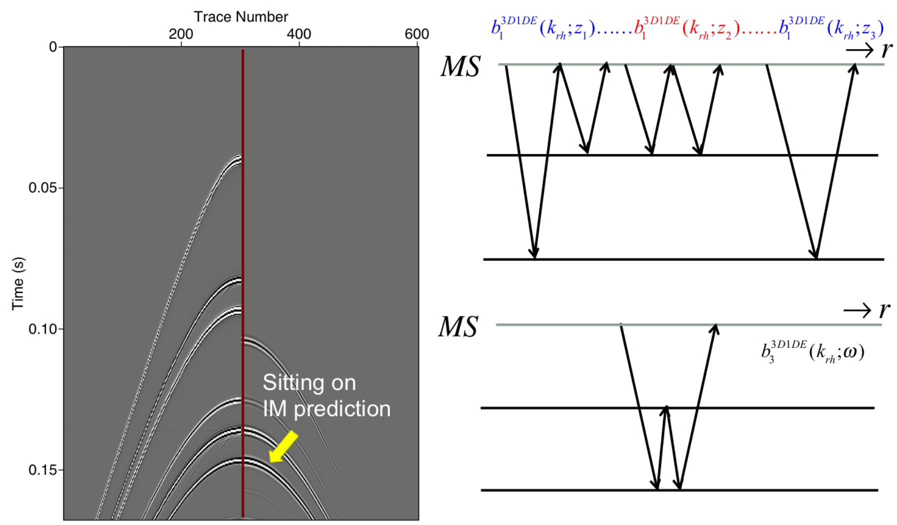

Figure 3.13: The analysis of events sitting on the internal multiple prediction generated by ISS internal multiple prediction algorithm using the input that contains free-surface multiple residues.

3.5 Incorporating a 3D point source in ISS IMA for a 2D subsurface

In this section, ISS internal multiple-attenuation algorithm for a 3D point source and a 3D subsurface is reduced for the data arising from a 2D subsurface. The modified 3D ISS internal multiple algorithm for a 2D subsurface presents the same data requirement and computational cost as a 2D ISS internal multiple attenuation algorithm (assuming a 2D line source and a 2D subsurface). Unlike the 2D source/2D earth algorithm, the modified/reduced algorithm preserves the effectiveness of predicting the amplitude and the shape of internal multiples for 3D point source data coming from a 2D subsurface. The similar discussions are named as 2.5D problems in history (Deregowski and Brown, 1983; Bleistein, 1986). The 2.5D problems have been presented and discussed by various authors in different contexts, including forward modeling (Deregowski and Brown, 1983; Liner, 1991; Williamson and Pratt, 1995; Miksat et al., 2008), migration (Esmersoy and Oristaglio, 1988) and inversion (Clayton and Stolt, 1981; Stolt and Benson, 1986; Bleistein, 1987). Different from the mentioned projects, this section focuses on a 2.5D ISS internal multiple-attenuation algorithm which can be reduced from a complete 3D algorithm.

3.5.1 Theory

The following sections will discuss the reduced 3D algorithm for the data from a 2D subsurface. For convenience, the superscript $2DE$ represents the 2D earth assumption for different sources (for example, $3D2DE$ represents a 3D point source and a 2D earth). The derivation starts from a complete 3D-internal-multiple attenuation algorithm, which is seen in equation (3.1), and then reduce the earth dimension from 3D to 1D.

3.5.1.1 The reduction of the source-side data by applying cross-line symmetry

3D data can be rearranged from $D(x_g, y_g, x_s, y_s; t)$ to $D(x_g, x_s, y_h, y_m; t)$, where $y_h = y_g - y_s$ (offset along y-direction) and $y_m = y_g + y_s$ (double the midpoint location along y-direction). Assuming the earth property is invariant along the y direction, then the dependence of data can be reduced from $D(x_g, x_s, y_h, y_m; t)$ to $D^{3D2DE}(x_g, x_s, y_h; t)$, which is independent of y_m. The Fourier transform over the 3D source/2D subsurface data, which is needed for the algorithm, can be seen as,

$$
\begin{aligned}
&D(k_{x_g}, k_{y_g}, k_{x_s}, k_{y_s}; \omega) \\
&= \iint dx_g dx_s \iint dy_g dy_s e^{i(k_{x_g}x_g + k_{y_g}y_g)} e^{-i(k_{x_s}x_s + k_{y_s}y_s)} \int dt e^{i\omega t} D^{3D2DE}(x_g, x_s, y_h, t) \\
&= \frac{1}{2} \int e^{ik_{y_h}y_h} D^{3D2DE}(k_{x_g}, k_{x_s}, y_h; \omega) dy_h \int e^{ik_{y_m}y_m} dy_m \\
&= D^{3D2DE}(k_{x_g}, k_{x_s}, k_{y_h}; \omega)(2\pi)\delta(k_{y_g} - k_{y_s}),
\end{aligned}
\tag{3.13}
$$

where $k_{y_h} = \frac{k_{y_g} + k_{y_s}}{2}$ and $k_m = \frac{k_{y_g} - k_{y_s}}{2}$. The data is independent of y_m and can come out of the integral. Consequently, the Fourier transform integral over y_m can produce a Dirac delta function in k_{y_m}. b_1 is defined as $b_1(k_{x_g}, k_{x_s}, k_{y_h}, k_{y_m}, q_g + q_s) = -2iq_s D(k_{x_g}, k_{x_s}, k_{y_h}, k_{y_m}; \omega)$. The uncollapsed Stolt migration b_1 is expressed as,

$$
\begin{aligned}
b_1(k_{x_g}, k_{y_g}, k_{x_s}, k_{y_s}; q_g + q_s) &= -2iq_s D(k_{x_g}, k_{y_g}, k_{x_s}, k_{y_s}; \omega) \\
&= -2iq_s D^{3D2DE}(k_{x_g}, k_{x_s}, k_{y_h}; \omega)(2\pi)\delta(k_{y_g} - k_{y_s}) \\
&= b_1^{3D2DE}(k_{x_g}, k_{x_s}, k_{y_h}; q_g + q_s)(2\pi)\delta(k_{y_g} - k_{y_s}),
\end{aligned}
\tag{3.14}
$$

where $q_i = \mathrm{sgn}(\omega)\sqrt{(\omega/c_0)^2 - k_{x_i}^2 - k_{y_i}^2}$. The symmetry factor in equation 3.14 is independent of $k_z = q_g + q_s$. In the following step, b_1 needs to be transformed back to the depth domain:

$$b_1^{3D2DE}(k_{x_g}, k_{x_s}, k_{y_g}, k_{y_s}; z) = b_1^{3D2DE}(k_{x_g}, k_{x_s}, k_{y_h}; z)(2\pi)\delta(k_{y_g} - k_{y_s}), \tag{3.15}$$

which is an uncollapsed Stolt migration. When the structure from 2D-earth symmetry in equation (3.14) is applied into current 3D ISS internal multiple attenuation algorithm in equation (3.1), the algorithm becomes,

$$\begin{aligned}
& b_3^{3D2DE}(k_{x_g}, k_{x_s}, k_{y_g}; \omega)\delta(k_{y_g} - k_{y_s}) \\
= & \frac{1}{(2\pi)^2} \iint_{-\infty}^{\infty} dk_{x_1} dk_{y_1} \iint_{-\infty}^{\infty} dk_{x_2} dk_{y_2} \\
& \times \int_{-\infty}^{+\infty} dz_1 b_1^{3D2DE}(k_{x_g}, k_{x_1}, k_{y_g}; z_1) e^{i(q_g+q_1)z_1} \delta(k_{y_g} - k_{y_1}) \\
& \times \int_{-\infty}^{z_1-\epsilon} dz_2 b_1^{3D2DE}(k_{x_1}, k_{x_2}, k_{y_1}; z_2) e^{-i(q_1+q_2)z_2} \delta(k_{y_1} - k_{y_2}) \\
& \times \int_{z_2+\epsilon}^{+\infty} dz_3 b_1^{3D2DE}(k_{x_2}, k_{x_s}, k_{y_2}; z_3) e^{i(q_2+q_s)z_3} \delta(k_{y_2} - k_{y_s}).
\end{aligned} \tag{3.16}$$

The lateral integrals $\iint dk_{y_1} dk_{y_2}$ is evaluated using the Dirac delta functions and then the algorithm is reduced to,

$$\begin{aligned}
& b_3^{3D2DE}(k_{x_g}, k_{x_s}, k_{y_h}; \omega) \\
= & \frac{1}{(2\pi)^2} \int_{-\infty}^{\infty} dk_{x_1} \int_{-\infty}^{\infty} dk_{x_2} \int_{-\infty}^{+\infty} dz_1 b_1^{3D2DE}(k_{x_g}, k_{x_1}, k_{y_h}; z_1) e^{i(q_g+q_1)z_1} \\
& \times \int_{-\infty}^{z_1-\epsilon} dz_2 b_1^{3D2DE}(k_{x_1}, k_{x_2}, k_{y_h}; z_2) e^{-i(q_1+q_2)z_2} \\
& \times \int_{z_2+\epsilon}^{+\infty} dz_3 b_1^{3D2DE}(k_{x_2}, k_{x_s}, k_{y_h}; z_3) e^{i(q_2+q_s)z_3},
\end{aligned} \tag{3.17}$$

where $k_{y_h} = k_{y_g} = k_{y_s}$ (evaluated by integrating over k_{y_g} on both sides), the vertical wavenumber $q_i = \text{sgn}(\omega)\sqrt{(\omega/c_0)^2 - k_{x_i}^2 - k_{y_h}^2}$ and $\epsilon_g = \epsilon_s$ (receivers and sources are located at the same depth).

In contrast to the complete 3D ISS internal multiple attenuator, which needs an areal coverage of receivers for each shot gather and also areal coverage of source locations, the reduced algorithm for a 2D subsurface requires an areal coverage of receivers for each pre-stack shot gather and also multiple sources along the inline direction (x-direction here).

3.5.1.2 The reduction of the receiver-side data using the stationary-phase approximation

People choose the 2D algorithm (which assumes a 2D line source) to process 3D data due to missing crossline data and efficiency. The line recording acquisition (multiple shot gathers along the inline direction) does not provide enough information to predict the internal multiple in a 3D algorithm. Even though we assume the earth varies the direction in (x, z), the areal coverage of receivers for each source and all the sources on one inline direction are required in equation (3.17), which shows $k_{y_g} = k_{y_s} = k_{y_h}$. That is because the algorithm is initially derived and calculated in the $(k_{y_g}, k_{y_s}; \omega)$ domain. To obtain each k_{y_h} (or k_{y_g}, k_{y_s}), the Fourier transform needs all receivers on the measurement surface. If the acquisitions are restricted to the central plane ($y_h = 0$ in this report) assuming a 3D point source, the asymptotic method will be applied to evaluate the summation of the wavenumber spectra only from the contribution of $k_{y_h} = 0$. The physics behind this approximation can be interpreted as that no out-of-plane wave arrivals are seen in the 2.5D data.

The uncollapsed Stolt migration $b_1^{3D2DE}(k_{x_g}, k_{x_s}, k_{y_h}; z)$ is related to the data,

$$b_1^{3D2DE}(k_{x_g}, k_{x_s}, k_{y_h}; z) = \frac{1}{2\pi} \int (-2iq_s) D(k_{x_g}, k_{x_s}, k_{y_h}; \omega) e^{-i(q_g+q_s)z} dk_z, \tag{3.18}$$

where $k_z = q_g + q_s$ and $q_i = \text{sgn}(\omega)\sqrt{(\omega/c_0)^2 - k_{x_i}^2 - k_{y_h}^2}$. The acquisition along $y_h = 0$ can provide only $D(k_{x_g}, k_{x_s}, y_h = 0; \omega)$. The rearranged Fourier transform seen in equation (3.18) as,

$$D(k_{x_g}, k_{x_s}, k_{y_h}; \omega) = \frac{1}{-2iq_s} \int b_1^{3D2DE}(k_{x_g}, k_{x_s}, k_{y_h}; z) e^{i(q_g+q_s)z} dz. \tag{3.19}$$

To fix the y-offset at $y_h = 0$, the k_{y_h} needs to be inverse Fourier transformed back to the space domain as,

$$D(k_{x_g}, k_{x_s}, y_h; \omega) = \frac{1}{2\pi} \int \int \frac{1}{-2iq_s} b_1^{3D2DE}(k_{x_g}, k_{x_s}, k_{y_h}; z) e^{i(q_g+q_s)z} e^{-ik_{y_h} y_h} dz dk_{y_h}. \tag{3.20}$$

This integration does not have a closed form solution; however, it involves all wavenumber along the y-direction. Using the stationary phase approximation with respect to k_{y_h}, the integral/summation over all the k_{y_h} spectrum is replaced by the single contribution at $\hat{k}_{y_h} = 0$ for $y_h = 0$ (seen in appendix D), where the $\hat{k}_{y_h}$ represents the stationary point. Setting $y_h = 0$ in equation (3.20) and applying the asymptotic approximation of integral $\int dk_{y_h}$ gives

$$D(k_{x_g}, k_{x_s}, y_h = 0; \omega) \approx \int \frac{e^{-i\frac{\pi}{4}}}{-2i\hat{q}_s} \sqrt{\frac{1}{2\pi z} \frac{\hat{q}_g \hat{q}_s}{\hat{q}_g + \hat{q}_s}} b_1^{3D2DE}(k_{x_g}, k_{x_s}, \hat{k}_{y_h} = 0; z) e^{i(\hat{q}_g+\hat{q}_s)z} dz, \tag{3.21}$$

where $\hat{q}_i = \text{sgn}(\omega)\sqrt{(\omega/c_0)^2 - k_{x_i}^2}$. A hat sign represents a variable that can be evaluated at a stationary point. The formula is rearranged to calculate the uncollapsed

Stolt migration at $k_{y_h} = 0$ as,

$$b_1^{3D2DE}(k_{x_g}, k_{x_s}, \hat{k}_{y_h} = 0; z)$$
$$\approx \sqrt{i2\pi z}\frac{1}{2\pi}\int(-2i\hat{q}_s)\sqrt{\frac{1}{\hat{q}_g} + \frac{1}{\hat{q}_s}}D(k_{x_g}, k_{x_s}, y_h = 0; \omega)e^{-i(\hat{q}_g+\hat{q}_s)z}d\hat{k}_z, \quad (3.22)$$

where $\hat{k}_z = \hat{q}_g + \hat{q}_s$ and $\hat{q}_i = \mathrm{sgn}(\omega)\sqrt{(\omega/c_0)^2 - k_{x_i}^2}$. Recall the formula in (3.17), which is reduced by crossline (y-direction) symmetry. When the wavenumber k_{y_h} is set to be zero, the equation is,

$$\begin{aligned} & b_3^{3D2DE}(k_{x_g}, k_{x_s}, \hat{k}_{y_h} = 0; \omega) \\ = & \frac{1}{(2\pi)^2}\int_{-\infty}^{\infty} dk_{x_1}\int_{-\infty}^{\infty} dk_{x_2} \\ & \times\int_{-\infty}^{+\infty} dz_1 b_1^{3D2DE}(k_{x_g}, k_{x_1}, \hat{k}_{y_h} = 0; z_1)e^{i(\hat{q}_g+\hat{q}_1)z_1} \\ & \times\int_{-\infty}^{z_1-\epsilon} dz_2 b_1^{3D2DE}(k_{x_1}, k_{x_2}, \hat{k}_{y_h} = 0; z_2)e^{-i(\hat{q}_1+\hat{q}_2)z_2} \\ & \times\int_{z_2+\epsilon}^{+\infty} dz_3 b_1^{3D2DE}(k_{x_2}, k_{x_s}, \hat{k}_{y_h} = 0; z_3)e^{i(\hat{q}_2+\hat{q}_s)z_3}, \end{aligned} \quad (3.23)$$

where $b_1^{3D2DE}(k_{x_g}, k_{x_s}, \hat{k}_{y_h} = 0; z)$ is calculated by equation (3.22). The internal multiple prediction result is expressed by $b_3^{3D2DE}(k_{x_g}, k_{x_s}, k_{y_h}; \omega)$ as,

$$D_3^{3D2DE}(k_{x_g}, k_{x_s}, y_h; t) = \frac{1}{(2\pi)^2}\iint \frac{b_3^{3D2DE}(k_{x_g}, k_{x_s}, k_{y_h}; \omega)}{-2iq_s}e^{-ik_{y_h}y_h}e^{-i\omega t}dk_{y_h}d\omega, \quad (3.24)$$

where $q_i = \mathrm{sgn}(\omega)\sqrt{(\omega/c_0)^2 - k_{x_i}^2 - k_{y_h}^2}$, D_3 is the internal multiple prediction in the $(k_{x_g}, k_{x_s}, y_h, t)$ domain, and k_{x_g}, k_{x_s} are omitted for convenience. Applying the same stationary phase approximation strategy with respect to k_{y_h} (appendix E),

$$D_3^{3D2DE}(k_{x_g}, k_{x_s}, y_h = 0; t) \approx \frac{1}{2\pi}\int\sqrt{\frac{-i\omega}{2\pi t c_0^2}}\frac{b_3^{3D2DE}(k_{x_g}, k_{x_s}, \hat{k}_{y_h} = 0; \omega)}{-2i\hat{q}_s}e^{-i\omega t}d\omega, \quad (3.25)$$

where $q_i = \mathrm{sgn}(\omega)\sqrt{(\omega/c_0)^2 - k_{x_i}^2}$. The complete procedure of the ISS internal multiple attenuation algorithm predicts D^{3D2DE} in the $(x_g, x_s, y_h; t)$ domain, which is approximated by equation (3.25).

For a 2D subsurface and a 3D point source, the ISS internal multiple attenuation is used by reducing a complete 3D algorithm. By applying an asymptotic approximation, the reduced algorithm only requires multiple shot gathers in the inline direction (x-direction), where sources and receivers are located at the $y_h = 0$ plane. This input requirement is the same as a 2D line source ISS internal multiple attenuator (equation (3.2)). Differences occur in the transforms of input and output data. After incorporating a 3D point source, the transforms of input (equation (3.22)) and output (equation (3.25)) contain several correction factors, as compared to Fourier transforms used by a 2D algorithm. The corrections have to be added to preserve the 3D point source assumption. The next section will discuss what is the relation between the derived formulas in this section and a conventional filter used in 2.5D studies.

3.5.2 Analysis

The $y_h = 0$ to $k_{y_h} = 0$ conversion filters (also understood as point-source to line-source conversion filters) have been presented by various authors in different contexts (Deregowski and Brown, 1983; Bleistein, 1986; Williamson and Pratt, 1995; Miksat et al., 2008). The simplest case is the difference between 2D and 3D Green's functions in a homogeneous acoustic medium. The frequency-domain solution (Fourier transformed Green's function) to the acoustic wave equation assuming a 3D point source can be expressed as (Aki and Richards, 2002)

$$G^{3D}(r;\omega) = \frac{1}{4\pi r} e^{\frac{i\omega r}{c_0}}, \tag{3.26}$$

where ω is the angular frequency, $r = \sqrt{x_h^2 + y_h^2 + z_h^2}$ and c_0 is the acoustic wave speed. The 2D frequency-domain Green's function solution for an acoustic homogeneous full space is given by Abramowitz and Stegun (1965):

$$G^{2D}(r';\omega) = \frac{i}{4} H_0^{(1)}(\frac{\omega r'}{c_0}), \tag{3.27}$$

where $H_0^{(1)}$ is the Hankel function of the first kind and zeroth order and r' is the distance between source and receiver in 2D ($r' = \sqrt{x_h^2 + z_h^2}$). Using the large argument approximation of the Hankel function (Morse and Feshbach, 1953), one obtains the asymptotic 2D-acoustic Green's function

$$G^{2D}(r';\omega) \approx \sqrt{\frac{c_0}{8\pi|\omega|r'}} e^{i(\frac{\omega r'}{c_0} + \frac{\pi}{4})}. \tag{3.28}$$

If we let $y_h = 0$ in equation (3.26), r reduces to $r' = \sqrt{x_h^2 + z_h^2}$. A simple derivation of the filter function is based on forming the ratio of the acoustic 3D and the asymptotic 2D Green's function as,

$$G^{2D}(r';\omega) = G^{3D}(r';\omega) \sqrt{\frac{i2\pi\sigma}{|\omega|}}, \tag{3.29}$$

where $\sigma = c_0 r'$ for an acoustic homogeneous medium. For a general heterogeneous medium, σ is given as the line integral of the velocity with respect to the arc length s of a ray trajectory (Miksat et al., 2008), $\sigma = \int c(s) ds$, where s is the arc length defined in a ray tracing method.

The correction filter in equation (3.22) can be compared to the conventional filter that transfers 3D source data to 2D line source data, which is in equation(3.29). The difference is that formula (3.17) corrects the source dimension in the image domain, instead of the temporal frequency domain ($\sqrt{r} \sim \sqrt{z}, \sqrt{\frac{1}{|\omega|/c_0}} \sim \sqrt{|\frac{1}{q_g} + \frac{1}{q_s}|}$). In this step, the correction filter $\sqrt{z}$ modifies the geometric spreading in wave propagation from $\sim \frac{1}{r}$ (3D) to $\sim \frac{1}{\sqrt{r}}$ (2D) in the depth domain. Also, $\sqrt{i|\frac{1}{q_g} + \frac{1}{q_s}|}$ adds a frequency scale and a $\frac{\pi}{4}$ phase shift on the 3D data. The filter we obtained in equation (3.22) is identical with the conversion filter from $k_{y_h} = 0$ (2D) to $y_h = 0$ (one 3D plane) for an acoustic homogeneous medium in equation (3.29).

For a 2D subsurface, the 3D ISS internal multiple attenuator can be reduced and performed as seen in equation (3.22), (3.23) and (3.25). The successive steps can be interpreted as three procedures. Firstly, the 3D point source data can be migrated and corrected to a 2D line source uncollapsed migration result (equation (3.22)). The second step applies the $b_1(\cdots, \hat{k}_{y_h} = 0; \omega)$ to a reduced 3D ISS internal multiple attenuator, where the wavenumber k_{y_h} was approximated to be zero. In fact, the attenuator was degraded to a 2D line source ISS internal multiple attenuator when $\hat{k}_{y_h} = 0$, because there was no wave propagation out of the $y_h = 0$ plane which provides a cylindrical wave front as in 2D propagation. Finally, equation (3.25) produced the prediction result in the space-time domain by inverse Fourier transforming the corrected $b_3(\cdots, \hat{k}_{y_h} = 0; \omega)/(-2i\hat{q}_s)$. The correction is a filter that transfers the 2D prediction back to 3D-source data.

3.6 Summary

A reduced and modified 3D source ISS internal multiple attenuator has been proposed for a 1D/2D subsurface, which enhances the realism of source dimension assumption. Numerical tests and analysis on synthetic 3D source/1D subsurface data illustrate that it is important to incorporate a more realistic source dimension in the ISS internal multiple attenuation. Incorporating a 3D point source can always effectively reduce the internal multiple. Using an internal multiple predictor that assumes a 2D line source can make the prediction significantly less effective with an extremely small amplitude. That was an interesting and surprising result for the important role that a 3D point source accommodation is effective for internal multiple prediction. Therefore, no matter what the earth dimension is 1D, 2D, or 3D, it is always essential to incorporate a 3D point source in multiple prediction since the real source is close to a localized 3D point source.

Furthermore, the subsequent ISS internal multiple prediction depends on the success of free-surface multiple removal. The results show that using input data with free-surface multiple residues can produce significant artifacts in the subsequent ISS internal multiple attenuation algorithm. Therefore, any step/prerequisite that cannot be carried out effectively can lead to negative consequences for subsequent processing. In this chapter, we demonstrate that incorporating a 3D source in a 1D ISS free-surface elimination algorithm is an important factor for both predicting free-surface multiples and in subsequent processing steps.

Chapter 4

An alternative ISS internal multiple elimination algorithm for the first-order internal multiples generated by the ocean bottom

This chapter finds an alternative way to remove attenuation factors. Instead of extracting $T_{01}T_{10}$ from the reflection data, those transmission factors can be found by velocity analysis at the ocean bottom for a typical marine case. For the internal multiple with a downward reflection at ocean bottom, to obtain $T_{01}T_{10}$ requires knowledge of the model down to and across the ocean bottom, independent on how deep and how many layers the first-order internal multiple travels through. With that information, it turns the internal multiple problem into the free-surface multiple case.

4.1 Introduction

The ISS provides all seismic processing techniques, for example, free-surface multiple removal and internal multiple removal, without the need to know earth properties. Among those methods, the ISS internal multiple attenuation algorithm (Araújo, 1994; Weglein et al., 1997) can predict the accurate time and approximate amplitude for all first-order internal multiples generated from all reflectors at once. When the multiple is completely isolated from other events, the energy minimization adaptive subtraction works by filling the gap between the prediction and the actual internal multiple plus, e.g., all pre-processing factors that are outside the assumed physics of the subsurface and acquisition. However, the primaries and multiples often interfere with each other in complex offshore and onshore plays where energy minimization fails (e.g., destructively interfering events). The reason is that the energy can increase after multiples are removed from interfering/overlapping events, which is against the assumption of energy minimization. In order to remove internal multiples for these circumstances, ISS elimination algorithm is needed and eliminating the internal multiples without damaging primary events becomes a challenging topic.

To address this challenging problem, Weglein (2014) proposed a three-pronged strategy, which aims to develop (1) ISS prerequisites by reference wave field prediction and data deghosting; (2) internal multiple elimination algorithm; (3) a new adaptive subtraction as a replacement for the energy minimization criteria. The method developed in this chapter belongs to the second aspect in this strategy.

Developing the ISS internal multiple elimination algorithm continued to draw high interest in processing history. To make the current internal multiple attenuator towards an eliminator, Weglein and Matson (1998) systematically studied the amplitude differences between predicted internal multiple (from the attenuation algorithm) and the true internal multiples. The difference is called an attenuation factor (which consists of extra transmission coefficients). An analytic example of the ISS internal multiple attenuator (Weglein and Matson, 1998) demonstrated that for a normal incident plane wave on a two-reflector model the predicted first-order internal multiple is $T_{01}T_{10}$ times the amplitude of actual internal multiple, where $T_{01}T_{10}$ are the transmission coefficients at the shallowest reflector. To produce an internal multiple eliminator from the ISS would require the removal of the $T_{01}T_{10}$ factor in terms of reflection data $1/(T_{01}T_{10}) = 1/(1-R_1^2) = R_1^2 + R_1^4 + \ldots$, where R_1 is the reflection coefficient at the shallowest reflector. That idea was first discussed in Ramírez (2007) and progressed in Herrera and Weglein (2012). Zou and Weglein (2014) and Zou et al. (2016) developed and advanced this idea into a comprehensive algorithm for 1D and 2D case, respectively. Those algorithms removed $T_{01}T_{10}$ in terms of reflection data and shared the unique advantage of the current ISS internal multiple attenuator, which is no need for subsurface information.

For a marine measurement containing a salt bed, recent progress in seismic processing can provide a well-estimated velocity/density model for down to and across the ocean bottom (but above the sub-salt body). For the internal multiple with a downward reflection at the ocean bottom, gives $T_{01}T_{10}$ with knowledge of the model above and below the ocean bottom, independent of how deep and how many layers the internal multiple travels through. It turns the internal multiple problem into the free-surface multiple case – the velocity/density properties where the downward reflections are known. With that information and inspired by the development of the Stolt extended Claerbout III migration, we utilize the known properties down to and across the ocean bottom in migration (the first step in ISS internal multiple prediction algorithm) to compensate for the $T_{01}T_{10}$. In this case, the ISS internal multiple attenuator can be made towards an eliminator.

This chapter will provide an alternative way to remove $T_{01}T_{10}$ from the first-order internal multiple predictions generated at the ocean bottom by applying the Stolt extended Claerbout III migration method, when the properties down to and across the ocean bottom are well known or estimated.

4.2 The 1D ISS internal-multiple attenuation algorithm and the idea of the ISS internal-multiple eliminator for the first-order internal multiple generated by the ocean bottom

The ISS internal multiple attenuation algorithm is pioneered by Araújo (1994) and Weglein et al. (1997), which is a multi-dimensional method for 1D, 2D, and 3D cases.

The 1D-normal incidence version of this algorithm was presented as following:

$$b_3(\omega) = \int_{-\infty}^{+\infty} dz_1 e^{2ikz_1} b_1(z_1) \int_{-\infty}^{z_1-\epsilon_2} dz_2 e^{-2ikz_2} b_1(z_2) \int_{z_2+\epsilon_1}^{+\infty} dz_3 e^{2ikz_3} b_1(z_3), \quad (4.1)$$

where $z_g = z_s = 0$, $k = \omega/c_0$, $b_1(z)$ is a constant velocity(c_0) Stolt-extended Claerbout III migration of a 1D-normal incidence plane wave data , $b_3(\omega)$ is the ISS internal multiple attenuator, and ϵ_i is a positive number that avoids self-interactions. This algorithm can predict the correct time and approximate amplitude of all first-order internal multiples at once without subsurface information. The amplitude difference between the predicted internal multiples (from attenuation algorithm) and actual internal multiples is called an attenuation factor (which consists of extra transmission coefficients).

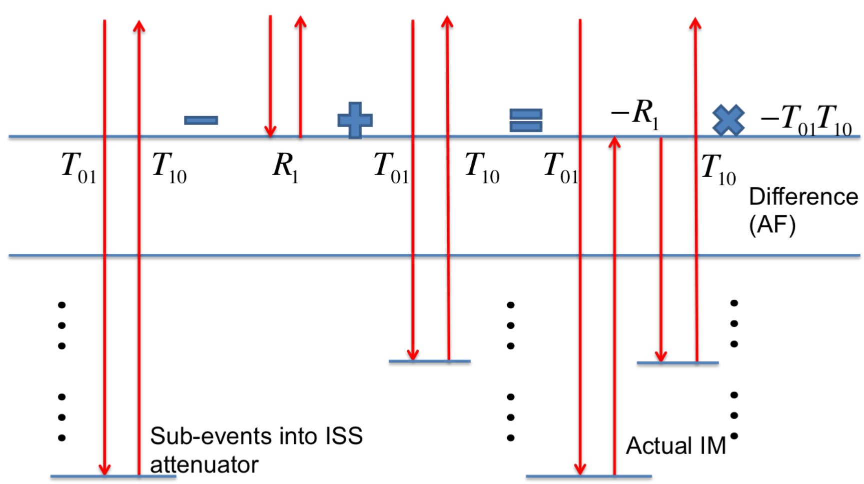

Figure 4.1: An example of the attenuation factor $T_{01}T_{10}$ of a first-order internal multiple generated at the shallowest reflector.

Figure 4.1 shows the general ISS procedure of predicting a first-order internal multiple generated at the shallowest reflector and why the prediction result is an attenuator. The ISS internal multiple attenuation algorithm can automatically select three primaries in the data to predict a first-order internal multiple. (The same procedure happens for predicting higher-order internal multiples, which will not be discussed in this chapter.) Since every sub-event on the left hand side experiences the phenomena making its way down to the earth then back to the receiver, the prediction result carries an extra attenuation factor - $T_{01}T_{10}$ - compared to the actual internal multiple in data. Removing this specific attenuation factor can provide an ISS internal multiple eliminator for all first-order internal multiples generated by the shallowest reflector, independent of how deep and how many layers the internal multiple travels through.

This ISS internal multiple eliminator can untangle the interfering or proximal primaries and first-order internal multiples, which is a challenging but common for data arising from a sub-salt structure. For this specific problem, the primaries that are reflected by a salt bottom can be overlapped/interfered by the internal multiples generated by the shallowest reflector. Fortunately, the subsurface properties above the salt body can be estimated. This provides the potential to develop the ISS internal multiple eliminator for internal multiples generated by the shallowest reflector. The input of the algorithm $b_1(z)$ is a Stolt-extended Claerbout III migration. Instead of using a constant velocity model, this chapter applies a well-estimated velocity model, which smoothly varies in depth, so the ISS internal multiple prediction can obtain $b_1(z)$. To preserve the actual amplitude of sub-events in data, a 1D phase-shift migration (Gazdag, 1978) is used to produce $b_1(z)$,

$$b_1(z) = \frac{2}{2\pi c_r(z)} \int d\omega e^{-2i\omega \int_0^z dz' \frac{1}{c_r(z')}} D(\omega), \tag{4.2}$$

where $z_g = z_s = 0$, $c_r(z)$ is the velocity depth-variable model. Data $D(\omega)$ is a plane wave in 1D-normal incidence. By applying the relation between phase-shift migration and de-migration, the ISS internal multiple attenuation algorithm using a smooth depth variable model $c_r(z)$ is obtained as,

$$\begin{aligned} b_3(\omega) = &\int_{-\infty}^{+\infty} dz_1 e^{2i\omega \int_0^{z_1} \frac{1}{c_r(z')} dz'} b_1(z_1) \int_{-\infty}^{z_1-\epsilon_2} dz_2 e^{-2i\omega \int_0^{z_2} \frac{1}{c_r(z')} dz'} b_1(z_2) \\ &\times \int_{z_2+\epsilon_1}^{+\infty} dz_3 e^{2i\omega \int_0^{z_3} \frac{1}{c_r(z')} dz'} b_1(z_3), \end{aligned} \tag{4.3}$$

where $z_g = z_s = 0$, b_3 is the ISS internal multiple attenuator.

The goal is to remove the attenuation factor, $T_{01}T_{10}$, from one of the outer $b_1(z)$s in equation (4.3) by using the known velocity model below the ocean bottom but above a salt body (high-velocity layer). Weglein et al. (2011a,b); Liu and Weglein (2014) pioneered the first wave-equation migration method – Claerbout III migration method, which can produce images that have the correct depth and amplitude (reflection coefficient at correctly located target) in a discontinuous medium. The $b_1(z)$ with $T_{01}T_{10}$ removed was obtained by a Claerbout III migration. The partially known $c_r(z)$ was chosen as the reference medium in scattering theory. Taking one step further, the ISS internal multiple eliminator under a depth-variable model $c_r(z)$ for the first-order multiples generated by the ocean bottom is proposed as,

$$\begin{aligned} b_3(\omega) = &\int_{-\infty}^{+\infty} dz_1 e^{2i\omega \int_0^{z_1} \frac{1}{c_r(z')} dz'} [b_1(z_1)]_{CIII} \int_{-\infty}^{z_1-\epsilon_2} dz_2 e^{-2i\omega \int_0^{z_2} \frac{1}{c_r(z')} dz'} b_1(z_2) \\ &\times \int_{z_2+\epsilon_1}^{+\infty} dz_3 e^{2i\omega \int_0^{z_3} \frac{1}{c_r(z')} dz'} b_1(z_3), \end{aligned} \tag{4.4}$$

where $z_g = z_s = 0$, $[b_1(z)]_{CIII}$ is a Claerbout III migration that removes the attenuation factor, $T_{01}T_{10}$, and $b_1(z)$ is a phase shift migration. Both $[b_1(z)]_{CIII}$ and

$b_1(z)$ are migrated with the same velocity model $c_r(z)$, so these two migration results provide the same migration results in terms of location.

4.3 1D Claerbout III migration with a WKBJ approximation

Liu and Weglein (2014) proposed the first wave-equation migration method - Claerbout III migration, which is an equally effective migration for all frequencies. With an accurate discontinuous medium, this method can produce images that have the correct depth and amplitude (that is, producing the reflection coefficient at the correctly located target) with primaries and internal multiples in the data. This result can compensate the attenuation factor as seen before in the input $[b_1(z)]_{CIII}$. However, the properties of shallow reflectors are required to be estimated or known.

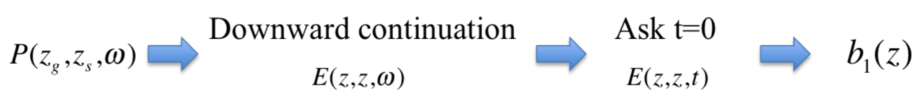

Figure 4.2: A simplified workflow of Claerbout III migration.

The basic workflow of the Claerbout III migration is seen in Figure 4.2. The downward continuations for both source and receiver side are obtained by applying the Green's theorem of wave-prediction.

4.3.1 Choosing a discontinuous medium

One choice is using the discontinuous medium as the reference medium (Liu and Weglein, 2014). $G_0^{DN}(z, z', \omega)$ represents a Green's function in a discontinuous medium which satisfies the Dirichlet and Neumann boundary conditions. If b is set as the deeper boundary location, then $G_0^{DN}(z, z' = b, \omega) = 0$ and $\partial G_0^{DN}(z, z', \omega)/\partial z'|_{z'=b} = 0$. The receiver-side downward continuation is seen as,

$$P(z, z_s, \omega) = \{P(z', \omega)\frac{\partial G_0^{DN}(z, z', \omega)}{\partial z'} - G_0^{DN}(z, z', \omega)\frac{\partial P(z', \omega)}{\partial z'}\}|_{z'=z_g}, \tag{4.5}$$

where z_g is the receiver depth and z is the target depth. Using the $P(z, z_s, \omega)$ in equation (4.5), the source-side downward continuation is:

$$E(z, z, \omega) = -\frac{\partial G_0^{DN}(z, z', \omega)}{\partial z'} + ik_s G_0^{DN}(z, z', \omega)P(z, z', \omega)|_{z'=z_s}, \tag{4.6}$$

where z_s is the source depth. Inverse Fourier transform $E(z, z, \omega)$ to the time-domain $E(z, z, t)$. And then ask the $t = 0$ to obtain $b_1(z) = E(z, z, t = 0)$. The result $b_1(z)$ can be analytically expressed as,

$$[b_1(z)]_{CIII} = R_1\delta(z - z_1) + R_2\delta(z - z_2) + \ldots, \tag{4.7}$$

where the R_i is the reflection coefficient from the i^{th} reflector and the z_i is the location of the i^{th} reflector. If the result in equation (4.7) can be applied in equation (4.4), the b_3 can eliminate the first-order internal multiple generated by the shallowest reflector.

4.3.2 Choosing a smooth medium

The other choice is applying a smooth velocity model which most industry migration methods use. We consider the waves actually travel in a smooth model, instead of a discontinuous model. Thereby, the downward continuations seen in equation (4.5) and (4.6) remain. The G_0^{DN} becomes a Green's function in smooth medium. However, the analytic form of Green's function only exists for several specific smooth models, for example, linear velocity model (Pekeris, 1946). For a general application, a WKBJ Green's function is used in this application. The WKBJ Green's function is an approximation solution for a medium with smooth variations. This WKBJ Green's function with double vanishing boundary conditions has been calculated and presented in Lin and Weglein (2016), which is named as $G_0^{WKBJ-DN}$. Consequently, the G_0^{DN} in equation (4.5) and (4.6) becomes a special WKBJ Green's function in a smooth model ($c_r(z)$) as

$$G_0^{WKBJ-DN}(z,z',\omega) = -\frac{\sqrt{c_r(z)c_r(z')}}{2i\omega}\{e^{-i\omega\int_{z'}^{z}\frac{1}{c_r(z'')}dz''} - e^{i\omega I(z,z')}\}, \tag{4.8}$$

where

$$I(z,z') = \begin{cases} \int_{z'}^{z}\frac{1}{c_r(z'')}dz'', & \text{if } z > z' \\ \int_{z}^{z'}\frac{1}{c_r(z'')}dz'', & \text{if } z < z'. \end{cases} \tag{4.9}$$

Since only up-going wave recorded by receivers works as input for ISS internal multiple removal algorithm (prerequisite), the Stolt-extended Claerbout III migration with a WKBJ approximation can be calculated and seen as,

$$[b_1(z)]_{CIII} = \frac{2}{2\pi c_r(0)}\int d\omega e^{-2i\omega\int_0^z dz'\frac{1}{c_r(z')}}D(\omega), \tag{4.10}$$

where $z_g = z_s = 0$ and $c_r(0) = c_0$. This result agrees with the WKBJ approximated result shown in Clayton and Stolt (1981). The equation (4.10) changes the amplitude by multiplying $c_r(z)/c_r(0)$ compared to phase-shift migration equation (seen in equation (4.2)).

The accurate amplitude (reflection coefficient) in Claerbout III migration (as seen in equation (4.7)) can still be achieved if attenuation factors are compensated by $c_r(z)/c_r(0)$ after (not at) the first reflector (e.g., ocean bottom) by a designed smooth velocity model.

A 1D-normal incidence example will be shown in the next section to exemplify the idea of ISS internal multiple eliminator using Claerbout III migration, with a designed smooth velocity model.

4.4 Numerical tests

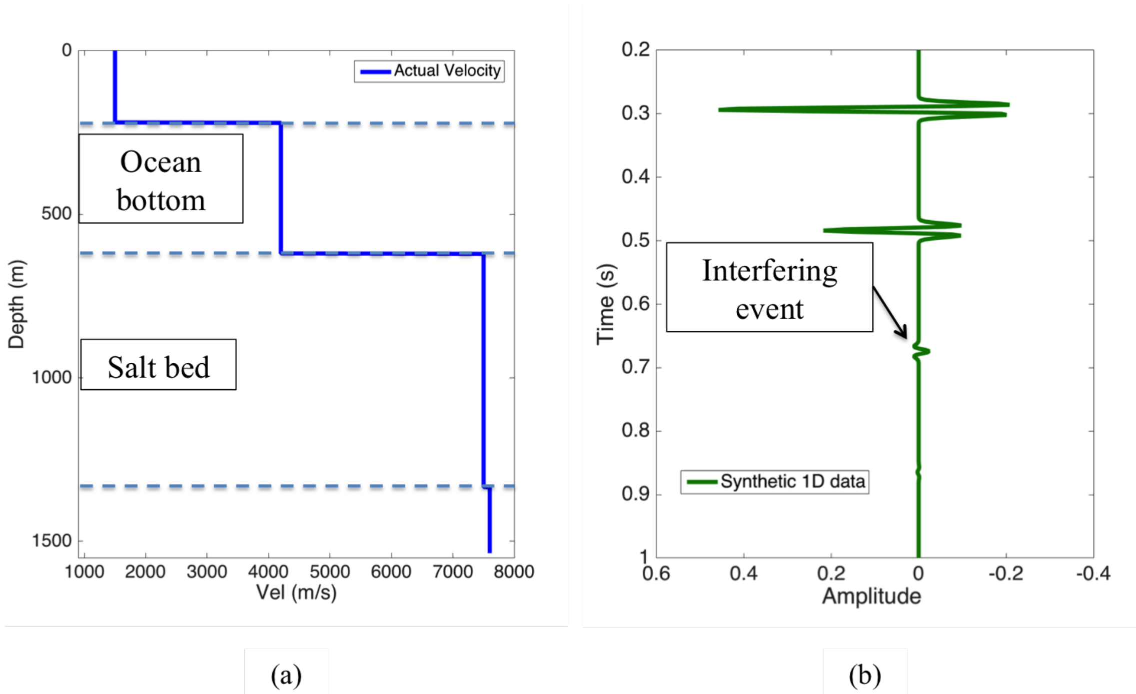

Figure 4.3: (a) 1D-velocity model and (b) 1D-synthetic data that is designed to have a third primary interfering with a first-order internal multiple for an internal multiple elimination test.

The synthetic 1D data (figure 4.3 (b)) generated by the reflectivity method using the velocity model (with a constant density $\rho = 1\ g/cm^3$) in Figure 4.3 (a). Source and receiver are located at $z_g = z_s = 0$. The 1D data contain three primary events and all internal multiple events, where the third event is the third primary interfered with a first-order internal multiple event generated by the water bottom, which changes the polarization of primary event. The goal of the test is to remove the first-order internal multiple generated by the shallowest reflector and simultaneously restoring the third primary event.

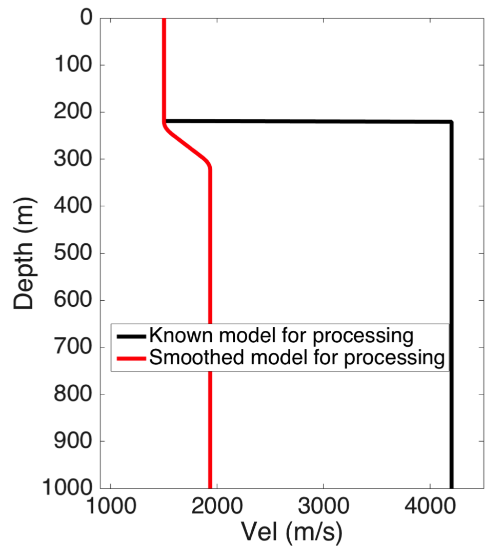

Figure 4.4: Known velocity model (black line) and designed smooth velocity model (red line) for migration.

Figure 4.4 provides the known velocity model for processing, black line and the designed smooth velocity model used for migration objective, red line. Two migration methods were performed to prepare the input for ISS internal multiple elimination algorithm (equation (4.4)).

One was the Claerbout III migration with a WKBJ approximation ($[b_1(z)]_{CIII}$), which is represented by a red line in figure 4.5. The smooth velocity was manipulated to make the amplitude compensation of the second primary event by removing $T_{01}T_{10}$. The other is the phase-shift migration seen by a blue line in Figure 4.5. From these results, we can see that both migration results provided the accurate locations and amplitudes (reflection coefficients) for the first primary event. For the events coming after the first primary, the attenuation factor is compensated only for CIII WKBJ migration. For example, the second primary in CIII migration carries the reflection coefficient R_2 instead of $R_2 T_{01} T_{10}$ in phase-shift migration.

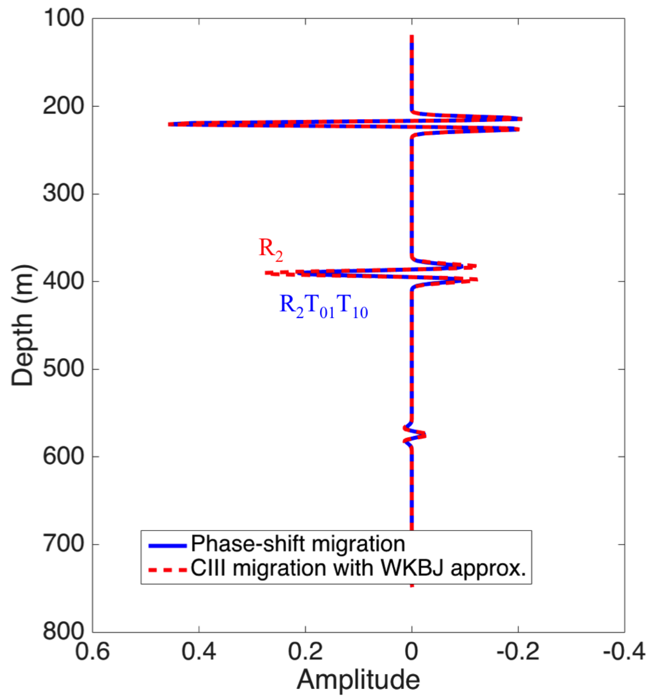

Figure 4.5: Stolt-extended Claerbout III migration with a WKBJ approximation (red line) and phase-shift migration (blue line).

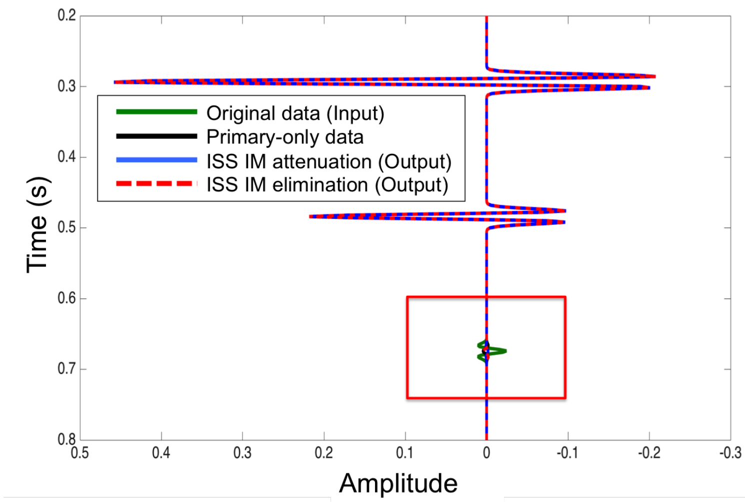

Figure 4.6: ISS internal multiple removed results, including input data (dark green line), primary-only data (black line), ISS internal multiple attenuated result (blue line), and ISS internal multiple eliminated result (dash red line).

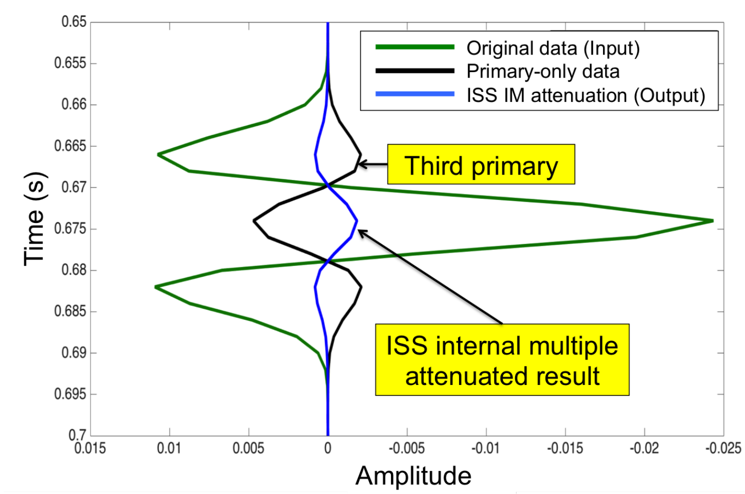

Figure 4.7: Large-scale plot of internal multiple attenuated result in the red box of figure 4.6.

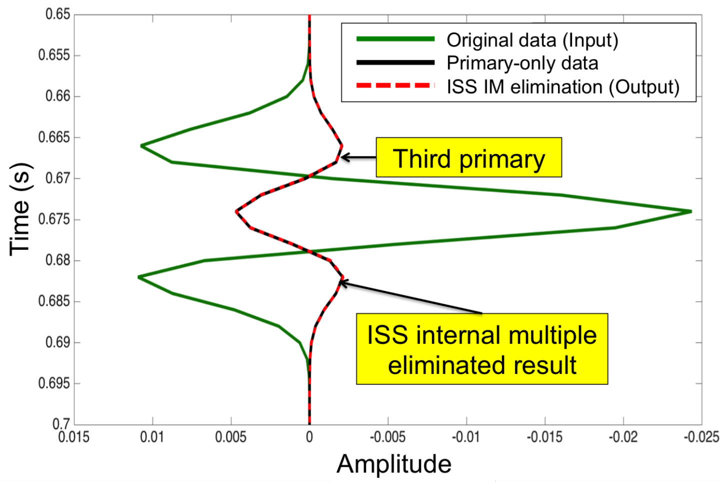

Figure 4.8: Large-scale plot of internal multiple eliminated result in the red box of figure 4.6.

The migration results in Figure 4.5 provide the capability to develop an ISS eliminator for the first-order internal multiples generated by the ocean bottom. Applying those migration results to equation (4.4), we can predict the target internal multiple (the first-order internal multiple generated by the ocean bottom) with accurate time and amplitude. Simple subtraction between the original data and prediction can eliminate the internal multiple interfering with the third primary event. Figure 4.6 shows input data, primary-only data, and internal multiple removals. Figure 4.7 and 4.8 are large scale plots of the interfering event. In figure 4.7, original data, simulated primary-only data, and current ISS internal multiple attenuated data is seen by dark green line, black line, and blue line, respectively. The internal multiple attenuated data has the same polarization as the overlapped event, which means the internal multiple still exists and overlaps with the third primary.

If the first-order internal multiple generated by the shallowest reflector can be accurately predicted, the result after multiple-removal should agree with the simulated primary-only data (black line) as seen in Figure 4.8 (elimination result, dash red line). Figure 4.8 illustrates that the new eliminator (dash red line) can eliminate the first-order internal multiple completely and restore the amplitude of the third primary event accurately.

4.5 Open issues for future work

- The internal multiple eliminator developed in this chapter assumes a well known/estimated simple model below the ocean bottom. However, if it is not easy/possible to extract the velocity/density information for the subsurface, the difference between approximately predicted first-order internal multiple (from attenuation algorithm) and identified actual multiples work as an indicator of inverting the velocity/density of the layer below the ocean bottom.
- The other ISS processing method – free-surface multiple elimination algorithm – works at one frequency at one time, which is equally effective for all frequencies. There is no doubt that the free-surface multiple prediction does not lose frequency. Instead of working frequency by frequency, the ISS internal multiple prediction involves a migration procedure. A migration with a high-frequency approximation (e.g., WKBJ approximation) may introduce low-frequency loss in the internal multiple prediction, which can lead to a loss of resolution.

4.6 Summary

The new approach proposed in this chapter contributes to the internal-multiple elimination task in the three-pronged strategy, which sets a higher bar for seismic processing to untangle the proximal/interfering primaries and internal multiples in complex off-shore or on-shore plays. The goal of this project is specified to add an alternative tool of developing an ISS internal multiple eliminator when the properties down to and across the ocean bottom can be well known/estimated. The numeric results shows that incorporating a Stolt-extended Claerbout III migration can make the current ISS internal multiple attenuator towards an eliminator for the first-order internal multiples downward reflected by the ocean bottom, independent of how deep and how many layers the internal multiple travels through.

Chapter 5

Conclusions

Two challenging issues in ISS multiple removal methods are covered and addressed in this dissertation. To deliver the promise of an ISS de-multiple method, a more realistic source dimension is used in an ISS free-surface multiple elimination algorithm and ISS internal multiple attenuation algorithm for a 1D/2D subsurface, improves the effectiveness of current multiple prediction/removal. Furthermore, to provide the capability beyond the current internal multiple attenuation algorithm, an alternative ISS internal multiple eliminator was developed to completely remove interfering internal multiples and restore the primary event.

First, the significance of incorporating a 3D point source was exemplified for the ISS free-surface multiple elimination algorithm. For 3D point source data coming from a 1D subsurface, the free-surface multiple prediction assuming a 2D line source was less effective due to the mismatch of source the dimension and the actual source dimension in the data. The free-surface events can be predicted by the mismatched

2D line source ISS free-surface elimination algorithm but the predictions carry a small amplitude and a distorted phase. When the events interfere, adaptive methods have difficulties in removing the multiples without harm to the primaries. In contrast, after the algorithm incorporates a 3D point source for a 1D subsurface, the prediction provides both an accurate time and an accurate amplitude of free-surface multiples, that can be used to eliminate the energy of all free-surface multiples in synthetic 3D source data. The effectiveness of ISS free-surface multiple elimination is increased by adding the physics of a realistic source for real 3D source data.

Second, in order to enhance the fidelity of internal multiple prediction, a 3D point source is also used in the ISS internal multiple attenuation algorithm. Similar to the summary in free-surface multiple removal, a frequently used 2D line source internal multiple attenuator for a 1D/2D subsurface produced a much less effective internal multiple prediction, which failed to attenuate internal multiples in 3D point source data due to small amplitudes. Incorporating a 3D point source makes ISS internal multiple attenuator effective. It provided accurate times and approximate amplitudes (in the same scale as data) of internal multiples. Ignoring a 3D source assumption for real data can result in a less effective multiple removal. In addition, successful internal multiple prediction depends on an effective free-surface multiple removal. The negative consequences of inputting free-surface multiple residues to the ISS internal multiple prediction were examined. There are at least three categories of artifacts that were identified and analyzed from unsatisfactory free-surface multiple removal.

Complex offshore and onshore plays set a higher bar to separate the proximal/interfering primaries and internal multiples. Third part of this dissertation provided a new way to eliminate the first-order internal multiples that are only downward reflected once by the ocean bottom. This approach was different from the ISS approach, which extracts the attenuation factor from reflection data without knowledge of subsurface properties. The goal of this project was to add an alternative tool in the ISS internal multiple eliminator when the properties down to and across the ocean bottom are well known or estimated. The numeric results showed that the proposed approach allowed the current ISS internal multiple attenuator to be an eliminator for the first-order internal multiples generated by the ocean bottom, independent of depth and numbers of layers the internal multiple travels through.

In summary, this dissertation contributes to the current capability of the ISS de-multiple methods by (1) adding a realistic 3D point source in several different ISS multiple-removal methods for a 1D/2D subsurface; (2) developing an internal multiple eliminator by using obtainable subsurface information for a certain class of internal multiples.

References

Abramowitz, M. and I. Stegun. “Handbook of mathematical functions: With formulas, graphs, and mathematical tables.” *Dover Publications* (1965).

Aki, K. and P. G. Richards. “Quantitative seismology.” *University Science Books* (2002).

Araújo, F. V. *Linear and non-linear methods derived from scattering theory: backscattered tomography and internal multiple attenuation.* PhD dissertation, Universidade Federal da Bahia, 1994.

Araújo, F. V., A.B. Weglein, P. M. Carvalho, and R.H. Stolt. “Inverse scattering series for multiple attenuation: An example with surface and internal multiples.” *64th Annual International Meeting, SEG, Expanded Abstracts* (1994): 1039–1041.

Baysal, E., D. Kosloff, and J. Sherwood. “Reverse time migration.” *Geophysics* 48 (1983): 1514–1524.

Bleistein, N. “Two-and-one-half dimensional in-plane wave propagation.” *Geophysical Prospecting* 34 (1986): 686–703.

Bleistein, N. “Two-and-one-half dimensional Born inversion with an arbitrary reference.” *Geophysics* 52 (1987): 26–36.

Carvalho, P. M. *Free-surface multiple reflection elimination method based on nonlinear inversion of seismic data*. PhD dissertation, Universidade Federal da Bahia, 1992.

Carvalho, P. M. and A. B. Weglein. “Wavelet estimation for surface multiple attenuation using a simulated annealing algorithm.” *64th Annual International Meeting, SEG, Expanded Abstracts* (1994): 1481–1484.

Claerbout, J. F. “Toward a unified theory of reflector mapping.” *Geophysics* 36 (1971): 467–481.

Clayton, R. W. and R. H. Stolt. “A Born-WKBJ inversion method for acoustic reflection data.” *Geophysics* 46 (1981): 1559–1567.

Deregowski, S. M. and S. M. Brown. “A theory of acoustic diffractors applied to 2-D models.” *Geophysical Prospecting* 31 (1983): 293–333.

Duquet, B., A. Chavanne, P. Poupion, M. Rowlands, B. Santos-Luis, and J. M. Ugolini. “Seismic Processing and Imaging in Central North Sea Area - Recents Advances and Remaining Challenges.” *75th EAGE conference* (2013).

Esmersoy, C. and M. Oristaglio. “Reverse-time wave-field extrapolation, imaging and inversion.” *Geophysics* 72 (1988): J53–J64.

Ferreira, A.S. “Internal multiple removal in offshore Brazil seismic data using the inverse scattering series.” *Master Thesis, University of Houston* (2011).

Fu, Q., Y. Luo, P. G. Kelamis, G. Huo, G.and Sindi, S.-Y. Hsu, and A. B. Weglein. "The inverse scattering series approach towards the elimination of land internal multiples." *80th Annual International Meeting, SEG, Expanded Abstracts* (2010): 3456–3461.

Fu, Q. and A. B. Weglein. "Internal multiple attenuation on Encana data." *84th Annual International Meeting, SEG, Expanded Abstracts* (2014): 4118–4123.

Gazdag, J. "Wave equation migration with the phase-shift method." *Geophysics* 43 (1978): 1342–1351.

Herrera, W. and A. B. Weglein. "Progressing amplitdue issues for testing 1D analytic data in leading order internal multiple algorithms." *M-OSRP annual report* (2012): 167–188.

Liang, H., C. Ma, and A. B. Weglein. "General theory for accommodating primaries and multiples in internal multiple algorithm: Analysis and numerical tests." *83th Annual International Meeting, SEG, Expanded Abstracts* (2013): 4178–4183.

Lin, X. and A. B. Weglein. "An alternative Inverse-Scattering-Series (ISS) internal multiple eliminator for the first-order internal multiples generated by the ocean bottom." *M-OSRP annual report* (2016): 121–140.

Liner, C. L. "Theory of a 2.5D acoustic wave equation for constant density media." *Geophysics* 56 (1991): 2114–2117.

Liu, F. and A. B. Weglein. "The first wave equation migration RTM with data consisting of primaries and internal multiples: Theory and 1D examples." *Journal of Seismic Exploration* 23 (2014): 357–366.

Luo, Y., P. G. Kelamis, Q. Fu, G. Huo, G. Sindi, S.-Y. Hsu, and A. B. Weglein. "Elimination of land internal multiple based on the inverse scattering series." *The Leading Edge* 30 (2011): 884–889.

Ma, C. and A. B. Weglein. "Including higher-order inverse scattering series terms to address a serious shortcoming/problem of the nternal-multiple attenuator: Exemplifying the problem and its resolution." *84th Annual International Meeting, SEG, Expanded Abstracts* (2014): 4124–4129.

Matson, K. and A. B. Weglein. "Removal of elastic interface multiples from land and ocean bottom data using inverse scattering." *66th Annual International Meeting, SEG, Expanded Abstracts.* (1996): 1526–1529.

McMechan, G. "Migration by extrapolation of time-dependent boundary values." *Geophysical Prospecting* 31 (1983): 413–420.

Miksat, J., T. M. Muller, and F.Wenzel. "Simulating three-dimensional seismograms in 2.5-dimensional structures by combining two-dimensional finite difference modelling and ray tracing." *Geophysical Journal International* 174 (2008): 309–315.

Morse, P. M. and H. Feshbach. *Methods of theoretical physics.* McGraw-Hill Book Co., 1953.

Pekeris, C. L. "Theory of propagation of sound in a half-space of variable sound velocity under conditions of formation of a shadow zone." *The journal of the acoustical society of America* 18 (1946): 295–315.

Ramírez, A. C. "1.-inverse scattering subseries for removal of internal multiples and depth imaging primaries;2.-Green's theorem as the foundation of interferometry and guiding new practical methods and applications." *PhD thesis, University of Houston* (2007).

Stolt, R. H. and A. K. Benson. *Seismic Migration: Theory and Practice*. Volume 5 of Seismic Exploration. Geophysical Press, 1986.

Terenghi, P., S.-Y. Hsu, A. B. Weglein, and X. Li. "Exemplifying the specific properties of the inverse scattering series internal-multiple attenuation method that reside behind its capability for complex onshore and marine multiples." *The Leading Edge* 30 (2011): 876–882.

Verschuur, D. J., A. J. Berkhout, and C. P. Wapenaar. "Adaptive surface-related multiple elimination." *Geophysics* 55 (1992): 1166–1177.

Weglein, A. B. "Multiple attenuation: Strategy that addresses current challenges." *E & P Magazine* 87 (2014): 132–135.

Weglein, A. B. "Multiple: signal or noise?." *Geophysics* 81 (2016): V283–V302.

Weglein, A. B., F. V. Araújo, P. M. Carvalho, R. H. Stolt, K. H. Matson, R. T. Coates, D. Corrigan, D. J. Foster, S. A. Shaw, and H. Zhang. "Inverse Scattering Series and Seismic Exploration." *Inverse Problems* (2003): R27–R83.

Weglein, A. B. and W. H. Dragoset. "Multiple Attenuation." *SEG* (2008).

Weglein, A. B., F. A. Gasparotto, P. M. Carvalho, and R. H. Stolt. "An Inverse-Scattering Series Method for Attenuating Multiples in Seismic Reflection Data." *Geophysics* 62 (November-December 1997): 1975–1989.

Weglein, A. B. and K. H. Matson. "Inverse scattering internal multiple attenuation: An analytic example and subevent interpretation." *SPIE Conference on Mathematical Methods in Geophysical Imaging* (1998): 108–117.

Weglein, A. B., R. H. Stolt, and J. D. Mayhan. "Reverse-time migration and Green's theorem: Part I- The evolustion of concepts, and setting the stage for the new RTM method." *Journal of Seismic Exploration* 20 (2011): 73–90.

Weglein, A. B., R. H. Stolt, and J. D. Mayhan. "Reverse-time migration and Green's theorem: Part II-A new and consistent theory that progresses and corrects current RTM concepts and methods." *Journal of Seismic Exploration* 20 (2011): 135–159.

Whitmore, D. "Iterative depth migration by backward time propagation." *53rd Annual International Meeting, SEG, Expanded Abstracts* (1983): 382–385.

Williamson, P.R. and R. G. Pratt. "A critical review of acoustic wave modeling procedures in 2.5 dimensions." *Geophysics* 60 (1995): 591–595.

Zhang, J. "Wave theory based data preparation for inverse scattering multiple removal, depth imaging and parameter estimation: Analysis and numerical tests of Green's theorem deghosting." *Ph.D. thesis* (2007): University of Houston.

Zou, Y., C. Ma, and A. B. Weglein. "The first inverse-scattering-series internal multiple elimination method for a multi-dimensional subsurface." *M-OSRP annual report* (2016).

Zou, Y. and A. B. Weglein. "An internal-multiple elimination algorithm for all reflectors for 1D algorithm, Part 1: Strengths and Limitations." *Journal of seismic exploration* 23 (2014): 393–404.

Appendix A

Transform integral variable from $\vec{r_g}$ to $\vec{r_h}$

The transformation from the integrand over the vector $\vec{r_g}$ to the other vector $\vec{r_h}$ can be obtained by Jacobian determinant. The definition of two vectors under cylindrical coordinate can be expressed by $\vec{r_g} = (r_g, \theta_g)$ and $\vec{r_h} = (r_h, \theta_h)$. Because of the $\vec{r_h} = \vec{r_g} - \vec{r_s}$, where the $\vec{r_g}$ is the location of receivers and the $\vec{r_s}$ is the location of sources, we have the relation between two vectors:

$$r_h = \sqrt{r_g^2 + r_s^2 - 2r_g r_s cos(\theta_g - \theta_s)} \tag{A.1}$$

$$\theta_h = \arctan(\frac{r_g sin\theta_g - r_s sin\theta_s}{r_s cos\theta_g - r_g cos\theta_s}). \tag{A.2}$$

The relation can be represented by a Jacobian determinant,

$$dr_h d\theta_h = |J| dr_g d\theta_g = \begin{vmatrix} \frac{\partial r_h}{\partial r_g} & \frac{\partial r_h}{\partial \theta_g} \\ \frac{\partial \theta_h}{\partial r_g} & \frac{\partial \theta_h}{\partial \theta_g} \end{vmatrix}. \tag{A.3}$$

Solve the determinant through the derivative values given by,

$$\frac{\partial r_h}{\partial r_g} = \frac{r_g - r_s cos(\theta_g - \theta_s)}{\sqrt{r_g^2 - r_s^2 - 2r_g r_s cos(\theta_g - \theta_s)}} \tag{A.4}$$

$$\frac{\partial r_h}{\partial \theta_g} = \frac{r_g r_s sin(\theta_g - \theta_s)}{\sqrt{r_g^2 - r_s^2 - 2r_g r_s cos(\theta_g - \theta_s)}} \tag{A.5}$$

$$\frac{\partial \theta_h}{\partial r_g} = \frac{b sin\theta_g - a cos\theta_g}{a^2 + b^2} \tag{A.6}$$

$$\frac{\partial \theta_h}{\partial \theta_g} = \frac{b r_g cos\theta_g - a r_g sin\theta_g}{a^2 + b^2}, \tag{A.7}$$

where $a = r_g sin\theta_g - r_s sin\theta_s$ and $b = r_g cos\theta_g - r_s cos\theta_s$. The J determinant can be calculated as,

$$|J| = \frac{\partial r_h}{\partial r_g}\frac{\partial \theta_h}{\partial \theta_g} - \frac{\partial r_h}{\partial \theta_g}\frac{\partial \theta_h}{\partial r_g} = \frac{r_g}{r_h}. \tag{A.8}$$

We obtain the relation between two integral variables, as

$$dr_h d\theta_h = |J| dr_g d\theta_g \tag{A.9}$$

$$r_h dr_h d\theta_h = r_g dr_g d\theta_g. \tag{A.10}$$

Appendix B

Dirac delta in the cylindrical coordinates

Prove the Dirac delta from a general formula,

$$\iint e^{i(\vec{k_{r1}}-\vec{k_{r2}})\cdot\vec{r_2}}d\vec{r_2} = (2\pi)^2\delta(k_{x1}-k_{x2})\delta(k_{y1}-k_{y2}). \tag{B.1}$$

Convert the Dirac delta on the right side from Cartesian coordinate to cylindrical coordinate, as

$$\delta(k_{r1}-k_{r2})\delta(\phi_1-\phi_2) = \left|\frac{\partial(k_{x1},k_{y1})}{\partial(\phi_1-\phi_2)}\right|\delta(k_{x1}-k_{x2})\delta(k_{y1}-k_{y2}) \tag{B.2}$$

$$\delta(k_{r1}-k_{r2})\delta(\phi_1-\phi_2) = \begin{vmatrix} cos\phi_1 & sin\phi_1, \\ -k_{r1}sin\phi_1 & k_{r1}cos\phi_1 \end{vmatrix} \times\delta(k_{x1}-k_{x2})\delta(k_{y1}-k_{y2}), \tag{B.3}$$

$$\frac{\delta(k_{r1}-k_{r2})\delta(\phi_1-\phi_2)}{k_{r1}} = \delta(k_{x1}-k_{x2})\delta(k_{y1}-k_{y2}). \tag{B.4}$$

The 2-dimensional Fourier transform over a constant can give us

$$\iint e^{i(\vec{k_{r1}}-\vec{k_{r2}})\cdot\vec{r_2}}d\vec{r_2} = (2\pi)^2\frac{\delta(k_{r1}-k_{r2})\delta(\phi_1-\phi_2)}{k_{r1}}. \tag{B.5}$$

Appendix C

Asymptotic Hankel transform

A general Hankel transform can be written as,

$$g(k) = 2\pi \int_0^{+\infty} f(r) J_0(kr) r dr, \tag{C.1}$$

where k is the Fourier conjugate of variable r, J_0 is the Bessel function of the first kind. The Hankel functions (Bessel function of the third kind) are defined by two linearly combining Bessel functions of the first (J_0) and the second kind (Y_0), i.e.,

$$H_0^+(z) = J_0(z) + iY_0(z), \tag{C.2}$$

$$H_0^-(z) = J_0(z) - iY_0(z), \tag{C.3}$$

where i is an imaginary unit, z is a general variable. Add equation (C.2) and (C.3) and then we have,

$$J_0(z) = \frac{H_0^+(z) + H_0^-(z)}{2}. \tag{C.4}$$

By substituting equation (C.4) into equation (C.1), the transform becomes,

$$
\begin{aligned}
& g(k) \\
&= 2\pi \int_0^{+\infty} f(r) \frac{H_0^+(kr) + H_0^-(kr)}{2} r dr && \text{(C.5)} \\
&= \pi \big(\int_0^{+\infty} f(r) H_0^+(kr) r dr + \int_0^{+\infty} f(r) H_0^-(kr) r dr \big) && \text{(C.6)} \\
&= \pi \big(\int_0^{+\infty} f(r) H_0^+(kr) r dr + \int_{-\infty}^{0} f(r) H_0^-(-kr)(-r) dr \big), && \text{(C.7)}
\end{aligned}
$$

where $f(r)$ is set to be a even function as $f(r) = f(-r)$ (e.g., data function from a 1D subsurface, which is symmetric along offset). Introduce two asymptotic forms of Hankel functions with $z = kr$ as,

$$H_0^+(kr) \sim \sqrt{\frac{2}{\pi kr}} e^{i(kr - \frac{\pi}{4})}, \tag{C.8}$$

$$H_0^-(kr) \sim \sqrt{\frac{2}{\pi kr}} e^{-i(kr - \frac{\pi}{4})}. \tag{C.9}$$

Apply these two asymptotic expressions into equation (C.7),

$$
\begin{aligned}
& g(k) \\
&\sim \int_0^{+\infty} \sqrt{\frac{2\pi r}{k}} e^{i(kr - \frac{\pi}{4})} f(r) dr + (-i) \int_{-\infty}^{0} f(r) \sqrt{\frac{2\pi r}{k}} e^{i(kr + \frac{\pi}{4})} dr && \text{(C.10)} \\
&\sim \int_0^{+\infty} \sqrt{\frac{2\pi r}{k}} e^{i(kr - \frac{\pi}{4})} f(r) dr + \int_{-\infty}^{0} f(r) \sqrt{\frac{2\pi r}{k}} e^{i(kr - \frac{\pi}{4})} dr && \text{(C.11)} \\
&\sim \int_{-\infty}^{+\infty} \sqrt{\frac{2\pi r}{k}} e^{i(kr - \frac{\pi}{4})} f(r) dr && \text{(C.12)} \\
&\sim \sqrt{\frac{2\pi}{ik}} \int_{-\infty}^{+\infty} \sqrt{r} e^{ikr} f(r) dr. && \text{(C.13)}
\end{aligned}
$$

Asymptotic inverse Hankel transform can be obtained in a similar way,

$$f(r)$$

$$= \frac{1}{2\pi} \int_0^{+\infty} g(k) J_0(kr) k dk \tag{C.14}$$

$$\sim \frac{1}{2\pi} \int_{-\infty}^{+\infty} \sqrt{\frac{k}{2\pi r}} e^{-i(kr - \frac{\pi}{4})} g(k) dk \tag{C.15}$$

$$\sim \frac{1}{2\pi} \sqrt{\frac{-1}{2i\pi r}} \int_{-\infty}^{+\infty} \sqrt{k} e^{-ikr} g(k) dk. \tag{C.16}$$

The asymptotic forward and inverse transforms, as shown in equation (C.13) and (C.16), are equivalent and can be exchanged by choosing different transform conventions. The specific convention in this appendix is chosen for consistency and the objective of comparing the Fourier and Hankel transforms. As an example, the Fourier transforms used in our derivation define $\int \cdots e^{ikx} dx$ as forward and $\int \cdots e^{-ikx} dx$ as inverse, but most numerical Fast Fourier transform functions set the convention reversely, including the numerical functions used in this dissertation.

Appendix D

Stationary-phase approximation to solve $D(\cdots, y_h = 0; \omega)$

Equation (3.20) cannot be solved as a closed form without any approximation. Omitting k_{x_g} and k_{x_s} in variable, equation (3.20) can be rewritten as,

$$D(\cdots, y_h; \omega) = \frac{1}{2\pi} \int \int \frac{1}{-2iq_s} b_1^{3D2DE}(\cdots, k_{y_h}; z) e^{i(q_g+q_s)z} e^{-ik_{y_h} y_h} dz dk_{y_h}, \tag{D.1}$$

where $q_i = \text{sgn}(\omega)\sqrt{(\omega/c_0)^2 - k_{x_i} - k_{y_h}}$. If we set a fixed plane at $y_h = 0$, the formula can be expressed as,

$$D(\cdots, y_h = 0; \omega) = \frac{1}{2\pi} \int \int \frac{1}{-2iq_s} b_1^{3D2DE}(\cdots, k_{y_h}; z) e^{i(q_g+q_s)z} dz dk_{y_h} \tag{D.2}$$

The integral with respect to dk_{y_h} can be approximated by a stationary phase assumption, which assumes a far-field recording and a smooth b_1^{3D2DE} with respect to k_{y_h}. In a far-field recording, the wave can be considered as propagating as a ray. The oscillating phase can be expressed as,

$$f(k_{y_h}) = (q_g + q_s)z = \mathrm{sgn}(\omega)\left(\sqrt{\frac{\omega}{c_0}^2 - k_{x_g}^2 - k_{y_h}^2} + \sqrt{\frac{\omega}{c_0}^2 - k_{x_s}^2 - k_{y_h}^2}\right)z. \tag{D.3}$$

The saddle point can be solved by finding the root of the equation,

$$f'(k_{y_h}) = \mathrm{sgn}(\omega)\left(\frac{-k_{y_h}}{\sqrt{\frac{\omega}{c_0}^2 - k_{x_g}^2 - k_{y_h}^2}} + \frac{-k_{y_h}}{\sqrt{\frac{\omega}{c_0}^2 - k_{x_s}^2 - k_{y_h}^2}}\right)z = 0. \tag{D.4}$$

Following the equation, the exponential can be stationary at $k_{y_h} = 0$. The second derivative of equation (D.3) at $\hat{k}_{y_h} = 0$ can be solved,

$$\begin{aligned} f''(\hat{k}_{y_h} = 0) = \mathrm{sgn}(\omega)\Bigg(& \frac{-1}{\sqrt{\frac{\omega}{c_0}^2 - k_{x_g}^2 - k_{y_h}^2}} + \frac{-1}{\sqrt{\frac{\omega}{c_0}^2 - k_{x_s}^2 - k_{y_h}^2}} \\ & + \frac{-k_{y_h}^2}{(\frac{\omega}{c_0}^2 - k_{x_g}^2 - k_{y_h}^2)^{3/2}} + \frac{-k_{y_h}^2}{(\frac{\omega}{c_0}^2 - k_{x_s}^2 - k_{y_h}^2)^{3/2}}\Bigg)z|_{\hat{k}_{y_h}=0} \\ = \mathrm{sgn}(\omega)\Bigg(& \frac{-1}{\sqrt{\frac{\omega}{c_0}^2 - k_{x_g}^2}} + \frac{-1}{\sqrt{\frac{\omega}{c_0}^2 - k_{x_s}^2}}\Bigg)z. \end{aligned} \tag{D.5}$$

If $z > 0$ and $\omega > 0$ are assumed in equation (D.5), then $f''(k_{y_h} = 0) < 0$, which defines the factor $e^{-i\frac{\pi}{4}}$. The integral formula in (D.1) can be approximated as,

$$D(\cdots, y_h = 0; \omega) \approx \int \frac{e^{-i\frac{\pi}{4}}}{-2i\hat{q}_s}\sqrt{\frac{1}{2\pi z}\frac{\hat{q}_g\hat{q}_s}{\hat{q}_g + \hat{q}_s}}\, b_1^{3D2DE}(\cdots, \hat{k}_{y_h} = 0; z)e^{i(\hat{q}_g+\hat{q}_s)z}dz, \tag{D.6}$$

where $\hat{q}_i = \mathrm{sgn}(\omega)\sqrt{(\omega/c_0)^2 - k_{x_i}^2}$. Similarly, if $z > 0$ and $\omega < 0$, the $f''(\hat{k}_{y_h} = 0)$ switches the sign and opening the absolute value can provide the same formula as shown in equation (D.6). Inverse Fourier transforming to obtain b_1^{3D2DE} gives,

$$\begin{aligned} & b_1^{3D2DE}(\cdots, \hat{k}_{y_h} = 0; z) \\ & \approx \sqrt{i2\pi z}\frac{1}{2\pi}\int(-2i\hat{q}_s)\sqrt{\frac{1}{\hat{q}_g} + \frac{1}{\hat{q}_s}}D(\cdots, y_h = 0; \omega)e^{-i(\hat{q}_g+\hat{q}_s)z}d\hat{k}_z, \end{aligned} \tag{D.7}$$

where $\hat{k}_z = \hat{q}_g + \hat{q}_s$, $\hat{q}_g = \mathrm{sgn}(\omega)\sqrt{(\omega/c_0)^2 - k_{x_g}^2}$ and $\hat{q}_s = \mathrm{sgn}(\omega)\sqrt{(\omega/c_0)^2 - k_{x_s}^2}$.

Appendix E

Stationary-phase approximation to solve $D_3(\cdots, y_h = 0; \omega)$

In a general 3D prediction, the internal multiple attenuator in $D_3(\cdots, y_h = 0; \omega)$ (omitting k_{x_g} and k_{x_s}) can be obtained as,

$$D_3^{3D2DE}(\cdots, y_h; t) = \frac{1}{(2\pi)^2} \iint \frac{b_3^{3D2DE}(\cdots, k_{y_h}; \omega)}{-2iq_s} e^{-ik_{y_h} y_h} e^{-i\omega t} dk_{y_h} d\omega, \qquad \text{(E.1)}$$

where the omitted variables are k_{x_g} and k_{x_s} and $q_i = \sqrt{(\omega/c_0)^2 - k_{x_i} - k_{y_h}}$. If we set the fixed plane at $y_h = 0$, the formula can be expressed as,

$$D_3^{3D2DE}(\cdots, y_h = 0; t) = \frac{1}{(2\pi)^2} \iint \frac{b_3^{3D2DE}(\cdots, k_{y_h}; \omega)}{-2iq_s} e^{-i\omega t} dk_{y_h} d\omega, \qquad \text{(E.2)}$$

The variable ω can be changed to $k_z = q_g + q_s$ as shown in Stolt and Benson (1986) (chapter 3, section 5), which provides the Jacobian term,

$$d\omega = \frac{c_0^2}{\omega} \frac{q_g q_s}{q_g + q_s} dk_z \qquad \text{(E.3)}$$

Formula (E.2) turns out to be,

$$D_3^{3D2DE}(\cdots, y_h = 0; t) = \frac{1}{(2\pi)^2} \iint \frac{b_3^{3D2DE}(\cdots, k_{y_h}; \omega)}{-2iq_s} e^{-i\omega(\cdots, k_{y_h}, k_z)t} \frac{c_0^2}{\omega} \frac{q_g q_s}{q_g + q_s} dk_{y_h} dk_z, \tag{E.4}$$

where for positive frequency (negative frequency can produce the same result at the last step)

$$k_z = \sqrt{\frac{\omega}{c_0^2}^2 - k_{x_g}^2 - k_{y_h}^2} + \sqrt{\frac{\omega}{c_0^2}^2 - k_{x_s}^2 - k_{y_h}^2}. \tag{E.5}$$

The integral with respect to dk_{y_h} can be approximated by a stationary phase assumption, which assumes a far-field recording and a smooth integral kernel with respect to k_{y_h}. The saddle point can be solved by finding the root of the equation,

$$\begin{aligned} f'(k_{y_h}) &= -\omega'(k_{y_h}) \\ &= -\frac{c_0^2}{\omega} k_{y_h} = 0. \end{aligned} \tag{E.6}$$

In equation (E.2), the exponential can be stationary at $\hat{k}_{y_h} = 0$. The second derivative of of equation (E.6) at $\hat{k}_{y_h} = 0$ can be solved,

$$f''(\hat{k}_{y_h} = 0) = -\frac{c_0^2}{\omega}. \tag{E.7}$$

Then $f''(k_{y_h} = 0) < 0$ for $\omega > 0$, which defines the factor $e^{-i\frac{\pi}{4}}$. The integral formula in (E.2) can be approximated as,

$$\begin{aligned} &D_3^{3D2DE}(\cdots, y_h = 0; t) \\ &\approx \frac{1}{2\pi} \int \sqrt{\frac{-i|\omega|}{2\pi t c_0^2}} \frac{b_3^{3D2DE}(\cdots, \hat{k}_{y_h} = 0; \omega)}{-2i\hat{q}_s} e^{-i\omega t} \frac{c_0^2}{\omega} \frac{\hat{q}_g \hat{q}_s}{\hat{q}_g + \hat{q}_s} d\hat{k}_z, \end{aligned} \tag{E.8}$$

where $\hat{q}_i = \mathrm{sgn}(\omega)\sqrt{(\omega/c_0)^2 - k_{x_i}^2}$. Change the integral variable back to $d\omega$,

$$D_3^{3D2DE}(\cdots, y_h = 0; t) \approx \frac{1}{2\pi} \int \sqrt{\frac{-i\omega}{2\pi t c_0^2}} \frac{b_3^{3D2DE}(\cdots, \hat{k}_{y_h} = 0; \omega)}{-2i\hat{q}_s} e^{-i\omega t} d\omega, \tag{E.9}$$

where $\hat{q}_i = \text{sgn}(\omega)\sqrt{(\omega/c_0)^2 - k_{x_i}^2}$.

If $\omega < 0$, the second derivative $f''(k_{y_h} = 0) = -\frac{c_0^2}{\omega}$ turns out to be a positive number, which provides the factor $e^{i\frac{\pi}{4}}$. The switched sign on i gives,

$$D_3^{3D2DE}(\cdots, y_h = 0; t) \approx \frac{1}{2\pi}\int \sqrt{\frac{i|\omega|}{2\pi t c_0^2}} \frac{b_3^{3D2DE}(\cdots, \hat{k}_{y_h} = 0; \omega)}{-2i\hat{q}_s} e^{-i\omega t} d\omega, \qquad \text{(E.10)}$$

Since $|\omega| = -\omega$, the formula remains,

$$D_3^{3D2DE}(\cdots, y_h = 0; t) \approx \frac{1}{2\pi}\int \sqrt{\frac{-i\omega}{2\pi t c_0^2}} \frac{b_3^{3D2DE}(\cdots, \hat{k}_{y_h} = 0; \omega)}{-2i\hat{q}_s} e^{-i\omega t} d\omega, \qquad \text{(E.11)}$$

where $\hat{q}_i = \text{sgn}(\omega)\sqrt{(\omega/c_0)^2 - k_{x_i}^2}$.